Wavelength Dependent Free-Carrier Absorption Pump/Probe Spectroscopy of Silicon

Wavelength Dependent Free-Carrier Absorption Pump/Probe Spectroscopy of Silicon

By:

Taz Colangelo

B.Eng.

A Thesis Submitted to the School of Graduate Studies in Partial Fulfillment of the Requirements for the Degree: Master of Applied Science

MASTER OF APPLIED SCIENCE (2021) MCMASTER UNIVERSITY

Department of Engineering Physics (Hamilton, Ontario)

TITLE: Wavelength Dependent Free-Carrier Absorption Pump/Probe Spectroscopy of Silicon

AUTHOR: Taz Colangelo, B.Eng.
(McMaster University)

SUPERVISOR: Professor Rafael N. Kleiman

NUMBER OF PAGES: 78

Abstract

The wavelength dependence on the free carrier absorption (FCA) cross-section has been explored using pump-probe spectroscopy. Until now the determination of the cross-section over a wavelength range using a completely optical method of carrier injection has yet to be done. For the first time, measurements are done at wavelengths less than 1000 nm which contributes to the overall measurement range of 935 to 2500 nm. In most cases, the work presented here agrees with literature values that have been reported at single wavelengths for optical injection methods. However, when compared to literature that uses non-optical injection methods, such as the introduction of dopants, there is a clear discrepancy between the methods. The cross-section for non-optical methods is roughly twice that when compared to the optical method though the curvature is consistent throughout. We believe this discrepancy comes from how carriers are scattering within doped and lightly doped materials. Since the process of FCA requires a momentum-conserving scattering event to occur, the dominant scattering mechanism must influence the magnitude of the FCA cross-section in some way. FCA upon optical injection is dominated by electron-hole scattering whereas FCA upon injection by dopants is facilitated through impurity scattering. As the doping level increases, not only will there be more carriers to collide with and scatter, but the process also introduces charge donor or acceptor atoms that can act as additional scattering sites resulting in a naturally higher cross-section.

Acknowledgments

When I started here at McMaster for my undergrad in 2014 in engineering, I would have never thought I would still be here seven years later. I enjoyed my time in undergrad in the engineering physics program which ultimately led to doing graduate school in the same department. My passion for optics and photovoltaics made it a no-brainer for me to pursue graduate school with Dr. Rafael Kleiman as my supervisor. I would like to thank Dr. Kleiman for giving me this opportunity and for all his guidance over these two and half years. He has been an excellent advisor who has led me to this point. His ability to always have great knowledgeable answers for every question you ask is something special.

I would like to thank everyone who has been in Dr. Kleiman's research group over the time I have been here. Most particularly would be Ruslan Khabibrakhmanov, David McShannon, Shuiawen Gao, and Kevin Boyd. Even though I never did get to work with Kevin Boyd, I have to thank him for the most because without all his previous work my work here wouldn't be possible. Thank you, Ruslan for passing the knowledge on and for helping me in the optic lab when I had barely had experience. Thank you, David McShannon for encouraging me to apply for graduate school and for your daily support.

I want to thank George Chiran for all his help in attempting to fix the OPO. He is a very kind and knowledgeable person from who I learned most of my optical skills from. Lastly, I would like to thank my family and my friends for their consistent support throughout this journey. I am very grateful to have met everyone that I have previously mentioned, and I wish them all the best!

Table of Contents

List of Figures

List of Tables

1. Introduction

In the work presented here, I show and examine the wavelength dependence of the free-carrier absorption (FCA) cross-section of silicon using pump-probe spectroscopy in the frequency domain. The method performed uses modulation free carrier absorption (MFCA) which can extract the recombination lifetime and AC signal amplitude values through a Lorentzian decay function. This can be further used to compute the cross-section values over a range of wavelengths using theoretically derived equations.

The wavelength range I achieved varied from 935 to 2500 nm. The higher wavelength range (1100-2500 nm) was made possible with the use of the Inspire HP100 optical parametric oscillator (OPO) with a thick silicon sample. For the lower wavelengths (935-1000 nm), a 3900s tunable Ti:Sapphire laser was used with thin silicon samples. Most notable is that the FCA cross-section values and the corresponding absorption coefficients reported over this lower wavelength range using a completely optical method like this have yet to be reported in literature until now.

With the use of MFCA pump-probe spectroscopy, the recombination lifetime of semiconductor materials such as silicon can be measured. The basic process involves using a laser as a pump source to excite electron-hole pairs (free carriers) up into the conduction band. This requires the pump laser's energy to be greater than the semiconductor's bandgap such that when a second laser beam is applied, a carrier (electron or hole) is excited from an already-excited state to another within the conduction band. This process is known as free carrier absorption. The second laser beam referred to as the probe can measure an induced FCA signal from the modulated pump beam. Sweeping through a range of modulation frequencies the signal from the probe displays a Lorentzian decay function which is curve fitted to obtain the recombination lifetime and AC probe signal amplitude.

The recombination lifetime is vital to assess the quality of materials, where high lifetime values are required to fabricate highly efficient and well-performing devices [1] [2]. In industry, it is important that the lifetimes be checked before fabrication to screen out any poor-performing materials. This ensures devices are fabricated with the best possible materials not wasting any supplies or time on anything less [3]. Further electronic

properties such as active defects, their density, and locations relative to the valence or conduction band edge can be determined by analyzing the lifetime results [4].

The FCA cross-section and the corresponding FCA coefficients are examined here in detail with focus on the wavelength dependence, as silicon solar cells operate over a wide range of wavelengths. FCA acts as a loss mechanism, particularly in heavily doped devices operating in the infrared where FCA competes with traditional band to band transitions. This energy is lost in the form of heat through thermalization in the upper energy levels of the conduction band.

FCA cross-section values reported in literature vary greatly and can be shown in the Baker-Finch et al. summary report [5]. These values are also only reported in the higher wavelength ranges. There are many reasons for these discrepancies; Baker-Finch claims there is a large experimental uncertainty as the cross-section is a function of many parameters [5]. Another reason has to do with the type of methods and samples used in the experiments.

Non-optical methods use samples with diffused dopants where the accuracy of the dopant profile is required to be high for a low uncertainty of the calculated FCA values [5]. However, for optical methods as presented here, samples are optically injected resulting in a much higher degree of precision as stated by Boyd who performed similar experiments [6]. He states the signal is only sensitive to the periodic change in the FCA population due to injection [6]. This limits the measurement uncertainty down to just one quantity rather than two quantities (the incident power, and the reflected/transmitted powers) for non-optical methods [6]. By examining my measured values presented in this report, I found that most optical reported values (including mine) agree with each other within error margins while all non-optical methods tend to show the most inconsistencies among themselves. However, when comparing the two methods there is a clear discrepancy among them.

2. Literature Review

2.1 Recombination Lifetime Characterization

In semiconductors, the process of recombination occurs when charge carriers are eliminated through the decay of electrons in the conduction band to holes in the valence band. In an equilibrium state where the number of electrons and holes are equal, there is no net transition from the conduction to valence band. However, when carriers are injected into the conduction and valence bands through the absorption of light, creating an electron-hole pair, the equilibrium state is temporarily lost. The average time it takes for this electron-hole pair to decay is the recombination lifetime. Since this parameter is vital to understanding the quality of the semiconductor material there have been many different techniques used to measure the lifetime.

The three main types of optical techniques include microwave photoconductance decay (μ-PCD), quasi-steady state photoconductance (QSSPC), and free-carrier absorption (FCA). The concept of each is similar but what makes them different is the state at which they operate and the method of probing the decaying signal of free carriers. The main operation states can be in the quasi-steady state (QSS) regime, frequency domain, or time domain. In this section, I will briefly describe the first two methods, while FCA will have its own overview in section 2.2 as it is the only method used in this work.

The basis of microwave photoconductance decay (μ-PCD) involves the monitoring of reflected microwaves, as the conductivity of materials change when they are optically injected with carriers [7]. As the free carrier density increases from injection, the conductivity also increases. This phenomenon is known as photoconductivity. The process utilizes microwave radiation that is incident on a sample inside of a cavity. Simultaneously, the sample is optically injected with carriers from a pulsed laser source. Due to photoconductivity, the conductivity increases causing the sample to reflect more of the microwaves. The change in reflectance of the microwaves is monitored as the photoconductivity returns to its equilibrium state. A decay constant can be extracted from

the measurement and in this case, it is equal to the recombination life. This linearity is only valid at low injection levels which heavily limits this technique [4].

In quasi-steady-state photoconductance (QSSPC), photoconductivity is the primary mechanism used with radio frequency (RF) radiation [7] [8]. In a quasi-steady-state, the optical source injects carriers at a slow enough rate such that the excess free-carrier population is always in equilibrium with the excitation. In the case of QSSPC, the lifetime is measured using only the absolute amplitude of the photoconductivity which is correlated to the free carrier density through the carrier mobility. By placing the sample in an RF inductance bridge, eddy currents are induced into the wafer causing a loss of energy proportional to the conductivity. A flash lamp source whose power is slowly controlled to decrease over time is monitored in relation to the change in photoconductivity. From this, and information gathered from a reference cell about the excitation rate, the lifetime can be determined.

2.2 FCA Characterization in Silicon

The FCA-based technique used in this work focuses on frequency-domain measurements, however, measurements made in the time-domain and quasi-steady-state are also possible. Frequency domain FCA is usually referred to as modulated free-carrier absorption (MFCA) and the primary goal of this technique is to determine the effective lifetime of material. The lifetime can verify the quality of the material and be used to calculate other important quantities. These methods were shown to work in the 1950s, however, popularity began to increase in the 1990s. This is when silicon photovoltaics started to become a viable and cost-effective option due to the decreasing cost of silicon [9]. The basic concept of the technique using a pump-probe setup has remained the same since the early work, though the advancements of equipment have made the measurements more reliable and accurate.

The use of a modulated pump beam in MFCA allows for a modulated excitation of carriers which can be monitored by a probe beam that is demodulated over a frequency range. The frequency dependency of the signal given by the probe beam is used to find the lifetime. In 1959, the earliest work of this was performed by Huldt who experimentally measured the lifetime of near-intrinsic germanium [10]. The pump was a tungsten strip lamp that was

modulated using an optical chopper and the probe was a monochromator emitting light in the mid-infrared range. The signal of the probe was measured using a Golay cell, a type of optoacoustic detector commonly used for infrared spectroscopy. Huldt's experiment involved changing the speed of the chopper which in turn changed the modulation frequency of the pump beam. From this, he observed a change in the probe beam signal which he used to calculate the lifetime of 165 μs. This was improved upon in 1964 by Nilsson who enhanced the sensitivity of the measurements by modulating the probe beam and by using a vacuum thermocouple sensor as the probe detector [11]. His results provided a 1D continuity equation for a square-wave excitation as well as lifetimes ranging from twenty to several hundred microseconds. However, both techniques were constrained to the modulation frequency range determined by the chopper's speed.

The earliest modern MFCA technique that closely resembles the one I use here was displayed in 1992 by Sanii et al. [12] [13]. This resemblance comes from using lasers as both sources, how the pump is modulated and how the probe is detected. The pump used is a 632 nm He-Ne laser and is modulated using an electro-optic modulator (EOM). The probe is another He-Ne laser at 3.39 μm and is detected using an InAs photodiode. A 300 μm thick silicon sample showed an effective lifetime of 221 μs which was in excellent agreement with the result of 223 μs using a photoconductive decay method. Sanii also presents a 1D continuity equation that provides a solution for a modulated pump. This is similar to Nilsson's solution for a square wave pump. It was shown by Boyd in this thesis that both solutions are in close resemblance to each other, however, Sanii's is more complex and provides a general basis for other possible configurations.

Using Sanii's solution it is possible to understand the transport and recombination of carriers in a semiconductor wafer by fitting the MFCA signal amplitude as a function of modulation frequency. From this, you can extract the bulk recombination lifetime, surface recombination velocity, and diffusion coefficients. It was shown experimentally and theoretically to great extent by Zang and Li that the diffusion coefficient can be determined by changing the distance between the pump and probe beams [14]. They showed a linear relationship between the probe signal and the separation between beams where the slope could be used to determine the diffusion coefficient.

Ren et al. used the basis of the 1D solution to extend it to a 3D model which considers diffusion along all three axes of the wafer [15]. Experimental data is fit to the model where the bulk lifetime, surface recombination velocity, and diffusion coefficient can be obtained. Since this model is very complex and does not produce a closed-form expression, Boyd derived the 3D continuity equation in position and time with a much more usable outcome. It closely follows and uses the 1D solution from Luke and Cheng [16].

MFCA can be used to determine the surface recombination velocity which is an important parameter used to determine the efficiency of solar cells. High surface recombination velocities lead to a lower generation of photocurrent which in turn leads to a decrease in overall efficiency. In 1992 Glunz et al. showed this by determining the effective lifetime through MFCA and the bulk lifetime from microwave photoconductivity decay [17]. Using these results, he was able to compute the surface recombination lifetime and velocity. Glunz et al. also went on to use MFCA to perform high-resolution lifetime mapping on a multi-crystalline silicon wafer. This proved to be very beneficial to determining the quality of these wafers due to large spatial variations in the lifetime of multi-crystalline silicon [18].

In 2020, it was shown by Gao that MFCA could be used to accurately measure the effective lifetime and diffusion coefficient simultaneously in silicon [19]. Gao used the model Boyd derived which accounts for 3D charge-carrier transport and recombination all throughout the wafer. The pump used in Gao's setup was a 1064 nm laser modulated using an EOM whereas the probe was a modulated LED emitting at 2050 nm. The probe signal was measured on an IR camera which provided frequency-based diffusion images of the laser spot over a frequency sweep. From this, the diffusion data can be used with the 3D continuity equation to obtain the diffusion coefficient and effective lifetime. The effective lifetime and diffusion coefficients were measured using the 3D model to be 32.8 ± 1.5 µs and 15.6 ± 0.7 cm^2/s respectively. This agreed with the measured lifetime of 33.5 ± 1.3 µs from MFCA and the theoretical value of 16 cm^2/s for silicon.

For the first time, the MFCA technique was used in a reflective mode in 2021 by Khabibrakhmanov [20]. In his setup, he measured the reflected probe beam from the sample instead of the usually transmitted part. Doing so, the light trapping enhancement

factor could be studied on double-side polished and double-side textured silicon wafers. This shows how MFCA can be used to calculate other important material parameters other than just the lifetime.

Khabibrakhmanov's setup also used a 1064 nm pump modulated using an EOM however his probe beam consisted of a 1550 nm laser. The setup is similar to that of Boyd's but the placement of detectors is different for reflective mode measurements. Reflective mode measurements were confirmed with transmitted mode values and proved to have great accuracy. For a relatively high lifetime, thick silicon sample (1500 μm) reflected beams values were measured to be 125.9 ± 0.7 μs compared to the transmitted beam of 124.6 ± 0.8 μs.

Using further analysis on the data collected from MFCA, the light-trapping enhancement can be studied to understand how the light propagates within the sample. A higher FCA signal indicates that light has remained within the sample for a longer period resulting in more absorption by free carriers. This leads to the determination of the light-trapping enhancement through a theoretical derivation which can be used to characterize the texturization quality of the surface of a wafer.

It is also possible to apply MFCA to more complex structures other than just silicon. It was shown by Suvanam et al. in 2015 that it can use to understand the interface and surface properties of 4H-silicon carbide substrates with a dielectric film [21]. This provided information about the density of traps at the surface as well as the interface between the silicon carbide and dielectric film. This was achieved by finding a relation between the FCA signal and capacitance-voltage values given from the trap density.

As mentioned at the beginning of this section, using quasi-steady-state (QSS) FCA is also possible for lifetime measurements as performed by Boyd in 2018 [22]. Traditional pump-probe can either be performed in the time or frequency domain. If monitoring the carriers in the time domain, the decay tracing out an exponential whereas in the frequency domain it is Lorentzian. Both are fit to extract the lifetime. Since the measurements performed in these methods are relative and only depend on the curve produced no extra calibration is required.

The QSS-FCA method is very similar to MFCA but instead of using the Lorentzian decay curve over a frequency sweep to find the lifetime, only a single point of the curve's amplitude is measured at low frequency. Calibration is required to determine the proportionality constant but minimizing the measurements to a single data point is an advantage over MFCA. Boyd suggests this technique could make QSS-FCA useful for high-accuracy wafer mapping. A model is also presented to quantify the relationship between the quasi-steady-state amplitude and the lifetime. This model is the basis for what is used in the work presented here and is shown that it can be applied to MFCA. The experimental setup closely resembles that of Boyd's with minor adjustments to configuration to better suit the purpose of my study.

2.3 Wavelength Dependence of FCA in Silicon

2.3.1 Overview

In this section, we will explore the wavelength dependence of FCA, more specifically the FCA cross-section (σ_{FCA}) and absorption coefficient (α_{FCA}). The FCA cross-section is a material constant that together with the effective lifetime and other experimental parameters determines the MFCA signal. With the cross-section and knowledge of the concentrations of free electrons the FCA coefficient can be calculated. This value and its wavelength dependence is important particularly for devices like solar cells operating over a wide range of wavelengths. FCA acts as a loss mechanism through thermalization, so knowing how readily light absorption occurs due to FCA over a wavelength range can be very beneficial to the design of solar cells.

The values for the FCA cross-section vary across literature. One reason for this could be the large experiment parameter space required for obtaining the cross-section [22]. It depends on the carrier density, carrier type, electron and hole concentrations, and probe wavelength. Another reason comes down to the sample and the mechanisms used to inject free carriers into the conduction band. Samples can be diffused with dopants to have fixed dopant levels, or they can be optically injected using light. In this work, 'non-optical methods' refers to work that uses samples with predetermined fixed dopant concentrations whereas optical methods use an optical source such as the pump laser in MFCA to inject

free carriers. As mentioned above, the FCA cross-section varies across literature, however, they do seem to stay consistent within the two separate regimes. The following sections will review these methods from literature separately and later in the experiential section they will be brought together to compare the results.

2.3.2 Non-Optical Methods

Non-optical methods are usually the most reported in literature with samples that have doping densities in excess of 10^{17} cm^{-3} [22]. Among the first work reported is from Schroder et al. in 1978 [23]. His prediction of the experimental wavelength FCA dependence uses the classical Drude theory of conductivity outlined by Smith in 1961 [24]. The Drude theory for bulk silicon relates the FCA coefficient as a function of density of the free carriers and wavelength squared. The equation also includes universal constants and material parameters such as the refractive index, effective mass, and mobility.

Since carrier concentration and mobility are highly dependent on temperature, the values Schroder et al. reports are only valid for a heavily doped condition where these qualities do not vary much with temperature. Experiments were performed at room temperature on uniformly doped samples with concentration values ranging from 10^{16}-10^{19} cm^3. The experimental data were taken over the wavelengths of 4, 5 and 10 µm but nowhere does it mention how these wavelengths were achieved or how the FCA coefficient was measured. The FCA coefficients were measured as a function of wavelength and carrier concentration to show an expected linear trend that agreed well with the Drude theory.

The model presented by Schroder et al. has become a common standard for silicon samples but due to its simplicity, it fails for heavily doped layers and in the high wavelength range. To improve upon this, Isenberg and Warta accounted for the sheet resistivity and the carrier concentration dependence on the refractive index and mobility [25]. Despite their initial improvement to the classical model, they opted to take a completely theoretical approach using the semi-classical theory to develop an FCA parameterization based on three fit parameters. Parameterization for both p- and n-type silicon using wavelengths of 1.2, 5 and 8 µm for doping densities as high as 10^{21} cm^{-3} were calculated using experimental data from literature.

This equation has also been applied to work relating to two-photon absorption (TPA) as shown by Fathpour et al. [26] and Sang et al. [27]. The phenomenon occurs when two photons are simultaneously absorbed to create a single excitation. Similar to FCA, this acts as a loss mechanism especially at high intensities where it has been seen to dominate. FCA may also induce TPA leading to additional loss. Finding the correlation between the two mechanisms is still an ongoing topic of study.

To generalize the Drude theory, an expression relates the absorption coefficient (α_{FCA}) to the product of a dimensionless parameterization coefficient (C_{FCA}), the doping concentration ($n\ or\ p$), and the wavelength raised to the exponent of an unknown constant ($\lambda^{\xi}\ or\ \lambda^{\varphi}$). For comparison's sake, the Drude theory with the use of well-known values for the universal constants and material parameters of silicon yield exponents of 2, and dimensionless coefficients of $C_{FCA,n} = 2.0 \times 10^{-18}$ and $C_{FCA,p} = 1.5 \times 10^{-18}$. Schroder et al. values for the exponents were also 2 while his dimensionless coefficient were $C_{FCA,n} = 1.0 \times 10^{-18}$ and $C_{FCA,p} = 1.5 \times 10^{-18}$ [23].

Green was the first to explore parametrization of the exponents ($\xi\ and\ \varphi$) for wavelengths less than 2.5 μm with a doping concentration of around 10^{18} cm^{-3} [28]. The values he achieved matched that of Schroder et al. for p-type silicon however for n-type he measured $C_{FCA,n} = 2.6 \times 10^{-18}$ with an exponent ξ = 3. The cubic behavior only in n-type silicon was explained by Green through the trends shown in experimentally determined absorption coefficients. For highly doped n-type silicon at longer wavelengths (λ > 5 μm) the trends are quadratic due to intra-band FCA and in the intermediate range (2 μm < λ < 4 μm) a characteristic hump from inter-band transitions can be seen which resembles a cubic function. This is displayed across all doping levels and is not observed for p-type silicon of similar doping levels.

Out of the previously mentioned literature only Isenberg and Warta presented data in a wavelength range of interest for solar cells, this was from their semi-classical approach with parametrizations at a single wavelength of 1.2 μm. Rüdiger et al [29], Xu et al [30]. and Baker-Finch et al. [5] were the firsts to capitalize on performing measurements over the wavelength range of λ = 1.0-2.0 μm.

Rüdiger et al. use the generalized Drude theory and apply it to reflection measurements on doped silicon wafers and assess their results with an optical model [29]. The samples are prepared on p-type float zone silicon with dopants of boron and phosphorus. The doping profiles showed surface dopant concentrations of approximately 10^{20} cm^{-3} which drops to 10^{16} cm^{-3} at a depth of 0.6 µm for boron and 0.5 µm for phosphorus. The FCA effect is enhanced using an inverted pyramid surface texture with a SiN_x anti-reflective coating.

The experimental setup uses a spectral photometer to measure the reflectance. Light reflected from the sample by a monochromatic source is detected using a lead sulfide photodiode. The diffuse reflected light is considered by placing the sample in a highly reflective sphere covered in Teflon. The results for the samples agree with their optical model (within 5%) which was set up in a numerical device simulator however both n- and p-type samples tend to slightly overestimate the FCA compared to the previously mentioned literature.

The final parameterization valid within the wavelength range of λ = 1.0-2.0 µm are $C_{FCA,n} = 1.8 \times 10^{-18}$ and $C_{FCA,p} = 2.6 \times 10^{-18}$with exponents of ξ = 2.6 and φ = 2.4 respectively [29]. Xu et al. took a very similar approach that of Rüdiger et al. performing parametrizations on silicon structures over a small wavelength range of λ = 1.0-1.2 µm [30]. However, only a limited number of samples were tested. The results for both n- and p-type showed cubic behaviour agreeing with Green's cubic result for n-type.

Lastly, Baker-Finch et al. use reflectance and transmittance dispersion measurements to obtain a parameterization for the FCA coefficient for a wavelength range of λ = 1.0-1.5 µm and doping concentrations between ~10^{18} and 3 x 10^{20} cm^{-3} [5]. Similar to Rüdiger et al., the n- and p-type samples were obtained through doping of silicon wafers using phosphorus and boron, respectively. Many samples were tested with different doping profiles, which had surface dopant concentrations for both n- and p-type around 10^{19} cm^{-3}.

The measurements were conducted using a spectrophotometer with the sample placed in an integrating sphere. An indium gallium arsenide (InGaAs) detector was used to collect and measure the reflected and transmitted beam. These could be compared to a reference beam to correct for any background noise. Results show that most of the previously

mentioned literature underestimates the FCA parametrizations for heavily phosphorus-doped silicon (>10^{18} cm^{-3}) though the values for boron tend to agree. The final parameterization valid within the wavelength range of λ = 1.0-1.5 µm are $C_{FCA,n} = 1.68 \times 10^{-14}$ and $C_{FCA,p} = 2.6 \times 10^{-17}$ with exponents of ξ = 2.88 and φ = 2.18 respectively [5].

2.3.3 Optical Methods

Optical methods reported in literature relating to the measurement of FCA are less common but more notably the majority of measurements for the FCA cross-section have only been reported at single wavelength values. The work in this paper capitalizes on this by exploring the FCA cross-section and coefficient through optical means (MFCA) over a wide range of wavelengths including wavelengths less than 1.0 µm.

Optical methods use optically injected carriers from a source, most commonly a laser which can generate a steady concentration of carriers. Among the earliest work performed was by Gauster and Bushell in 1970 on single crystal silicon wafers [31]. The pump used to induce absorption was a 1064 nm Nd^{3+} laser and the probe used to monitor and generate the FCA mechanism was a flash lamp at a wavelength range of λ = 1.2-2.7 µm. Measurements were carried out in the time-domain which showed an exponential relation between the transmitted light and laser pulse energy density from the pump. The detector used to measure the transmitted light was a photodiode with a fast response time. The cross-section value was reported at λ = 1.06 µm to be $\sigma_{FCA} = 4.9 \times 10^{-18}$ cm^2 and revised for λ = 2.6 µm to be $\sigma_{FCA} = 1.7 \times 10^{-17}$ cm^2.

An experimental method without the use of a probe beam was carried out by Svantesson and Nilsson [32]. It used a pulsed Nd: YAG laser at λ = 1.06 µm on silicon samples of various thicknesses from the same ingot. With only the measured attenuation they showed it was possible to measure the inter-band absorption coefficient, the FCA cross-section, and concentration of generated carriers in silicon.

The incident beam was attenuated using carefully calibrated neutral glass filters. A beam splitter was used to direct a portion of the incident beam into a photomultiplier for

measurements regarding the incident photon density. For the experiments, the photon densities ranged from 6 x 10^{15} to 3 x 10^{18} photon/cm^2. Another photomultiplier was placed behind the sample to measure the transmitted beam. Six samples were tested with thicknesses of 0.53, 0.70, 1.10, 1.46, and 1.69 mm. The cross-section value was reported at λ = 1.06 μm to be $\sigma_{FCA} = 4.9 \times 10^{-18}$ cm^2 which agreed exactly with Gauster and Bushell.

Linnros performed a time-domain FCA pump-probe experiment primarily for recombination lifetime characterization but also determined the FCA cross-section at his probe wavelength [33]. The pump beam used was an Nd: YAG laser at λ = 1.06 μm in conjunction with a HeNe probe emitting at λ = 3.39 μm on an InAs detector. The measurements were based on the exponential decay of the carrier density over time which enabled the extraction of lifetimes. The densities were determined using the incident, reflected, and transmitted beams which ranged from 10^{14}–10^{17} cm^{-3}. The cross-section value was reported to be $\sigma_{FCA} = 2.5 \times 10^{-17}$ cm^2 for a probe wavelength of λ = 3.39 μm.

Another time-domain pump-probe experiment was performed by Meitzner et al [34]. The experiment's focus is to determine the internal quantum efficiencies for various pump wavelengths. However, in doing so the FCA cross-section is required for the calculation. The experimental setup uses one Ti:Sapphire laser emitting at 800 nm. The beam is split into the pump and probe. The pump beam produces 400 nm and 267 nm beams after being sent through beta-barium borate crystals (BBO) which undergo second and third harmonic generation. The probe turns into 1510 nm light after optical parametric amplification and is delayed a few nanoseconds relative to the pump beam. Detectors are used to collect the transmitted and reflected probe beams from the sample. The change in transmitted and reflected light is used to determine the FCA. A cross-section value $\sigma_{FCA} = 1.69 \times 10^{-17}$ cm^{2}was determined for the wavelength of λ = 1510 nm.

Lastly, work performed by Boyd [22] uses QSS-FCA for lifetime measurements resulting in the calculation of the FCA cross-section. The general measurement technique was described at the end of section 2.2 previously. A set of equations derived by Boyd leads to a linear relationship between the normalized FCA signal and the product of the FCA cross-

section, the lifetime, and material constants. Since the FCA signal is proportional to the pump power, the pump power was varied from 10 to 650 mW while extracting lifetime measurements for each pump power. The normalized FCA signal divided by the material constant was then plotted against the recorded lifetime to prove the linearity. The slope resulted in the FCA cross-section of $\sigma_{FCA} = 4.71 \times 10^{-10}$ μm^2 for a wavelength of λ = 1550 nm.

From this literature review we can see the motivation behind this work; to capitalize on determining the FCA cross-sections using optical injection through MFCA over a wide range of wavelengths including ones that have never been used before.

3. Theoretical Background

3.1 Absorption Mechanisms in Semiconductors

The two main absorption mechanisms in semiconductors are referred to as inter- and intra-band transitions. Both mechanisms are involved with MFCA and the calculation of the effective lifetime in this work. An inter-band transition, also known as a band-to-band transition is the most common form of absorption in semiconductors. This occurs when the semiconductor material absorbs light, allowing for an electron in the valence band to be promoted or excited up into the conduction band. The process involves the addition of an electron in the conduction band and a hole in the valence band. However, for this process to occur the absorbed light must have energy equal to or greater than the material's characteristic bandgap. If the energy of the photon is less than the bandgap, the material will be transparent to the photon, causing complete transmission and no absorption. If the photon energy is greater than the bandgap, absorption will occur, but the extra energy will be lost to thermalization.

In silicon, the bandgap is approximately 1.1 eV which converts to a photon wavelength of 1.13 μm. Silicon is an indirect semiconductor meaning the top of the valence band and the bottom of the conduction do not line up in momentum space. This leads to an additional requirement to complete an inter-band transition for indirect semiconductors. Since light has low momentum compared to its energy, the additional requirement must involve a

momentum-conserving collision with a phonon to complete the transition. Doing so leads to a probability of the overall transition not occurring if a phonon is not present. This results in a lower absorption coefficient for indirect semiconductors compared to direct. Direct semiconductors such as gallium arsenide (GaAs) have their band edges aligned meaning no additional step is required for an inter-band transition to occur.

Once a carrier has reached the conduction band through an inter-band transition, there is a possibility of a further transition to occur within the same band. This is known as an intra-band transition or free carrier absorption (FCA). This process occurs when an already excited electron is excited again within the same band through the absorption of light. Due to the parabolic nature of the conduction band, in order for a carrier to move up in the band, it requires not only a photon but also a momentum-conserving collision.

This collision may be in the form of lattice scattering, electron-hole scattering, or scattering from a charged impurity [35]. The type of scattering depends on the materials and if it has been doped or not. Samples with diffused dopants undergo impurity scattering, the process of free carriers interacting with charge donor or acceptor atoms. In lightly doped samples where the free carriers are optically injected, the main scattering mechanism is electron-hole scattering in which free carriers interact with each other. This could be the reason for the discrepancy in FCA among the different samples being used.

The FCA coefficient can be described using the Drude theory of conductivity [24]:

$$\alpha_{FCA} = \frac{q^3\lambda^2}{4\pi^2\varepsilon_0 c^3 n}\left[\frac{n}{m_n^{*2}\mu_n} + \frac{p}{m_p^{*2}\mu_p}\right] \tag{3.1}$$

where q represents the elementary charge, λ is the wavelength of absorbed light, ε_0 is the permittivity of free space, c is the speed of light, n is the material's refractive index, n and p are the free carrier concentrations for electrons and holes respectively, m_n^* and m_p^* are the effective masses for electrons and holes respectively and lastly μ_n and μ_p are the carrier mobilities for electrons and holes respectively.

The assumption is made that electrons and holes are generated in a one-to-one ratio allowing for carrier concentrations to be equal, $n = p$. Equation (3.1) can be written now

in terms of a single concentration with a proportionality constant made up of universal constants and material parameters. This material constant is the FCA cross-section σ_{FCA}.

$$\alpha_{FCA} = \sigma_{FCA} n \tag{3.2}$$

For our work it is more useful to rewrite (3.2) using the wavelength dependent term:

$$\alpha_{FCA} = C_{FCA} \lambda^{\xi} n \tag{3.3}$$

where C_{FCA} is the FCA parametrization coefficient, and ξ represents the exponent determined through parameterization of the wavelength-dependent term. In the case of the classical Drude theory $\xi = 2$ but as described in section 2.3.1 regarding other literature and in this work that ξ does is not found to be 2 for the best agreement. To find the wavelength dependence on the σ_{FCA} we can set equation (3.2) equal to (3.3) which results in a parameterization fitting equation:

$$\sigma_{FCA} = C_{FCA} \lambda^{\xi} \tag{3.4}$$

Equation (3.4) will become useful in section 4 when used to fit experimental data and to compare it to literature described in section 2.3.2.

3.2 Recombination Mechanisms in Semiconductors

Recombination in semiconductors occurs when an electron in the conduction band spontaneously combines with a hole in the valence band. The electron-hole pair is annihilated in the process. The rate of recombination of excess carriers is an exponential relation that results in the extraction of a time constant in the decay characteristic curves. The time constant is referred to as the recombination lifetime which describes the average time it takes for thermal equilibrium to be reached through the recombination of excess carriers within the conduction band.

The types of recombination mechanisms are categorized into intrinsic and extrinsic processes. An intrinsic process occurs directly and cannot be altered or eliminated. The process depends on the dispersion of excess energy released by the recombination of an electron-hole pair. An extrinsic process occurs indirectly and uses traps or defects within the semiconductor to aid in the process. Traps are introduced through impurity atoms so

these processes can be reduced by using very pure materials. Radiative and Auger recombination are intrinsic processes whereas Shockley-Read-Hall (SRH) and surface recombination are extrinsic processes.

In this work using MFCA, the total effective lifetime τ is measured and is described as the reciprocal sum of the individual mechanism as shown in the equation below:

$$\frac{1}{\tau_b} = \frac{1}{\tau_{rad}} + \frac{1}{\tau_{Aug}} + \frac{1}{\tau_{SRH}} \tag{3.5}$$

$$\frac{1}{\tau} = \frac{1}{\tau_b} + \frac{1}{\tau_s} \tag{3.6}$$

where τ_b, τ_{rad}, τ_{Aug}, τ_{SRH}, and τ_s are the bulk, radiative, Auger, Shockley-Read-Hall (SRH), and surface recombination lifetimes, respectively. The inverse bulk recombination is the sum of all the inverse lifetimes that occur within the semiconductor, separate from the surface recombination process.

Radiative recombination is a direct process of electron-hole annihilation. As the electron decays down to the unoccupied state (hole) in the valence band it releases a photon with energy equal to that of the material's bandgap. For direct semiconductors where the band edges line up, this process tends to dominate as it is a 1-step transition. However, for indirect semiconductors, a momentum conserving event is required to complete the full transition. This introduces the probability that the transition will not occur if this condition is not met causing radiative recombination to be lower in indirect semiconductors [4]. The radiative recombination lifetime can be written as:

$$\tau_{rad} = \frac{1}{B(n_0 + p_0 + \Delta n)} \tag{3.7}$$

where B is a rate constant, n_0 and p_0 are the thermal equilibrium carrier densities for electrons and holes respectively, and Δn is the density of free carriers above the equilibrium concentration.

Auger recombination is the process of electron-hole recombination but instead of transferring its energy as a photon as in a radiative process, the energy is transferred to a free carrier within the conduction band. The free carrier is excited to a higher energy state

and any excess energy results in the release of phonons. At low carrier densities, the Auger lifetimes are long as they are inversely proportional to the free carrier density as shown in the relation below [4]:

$$\tau_{Aug} = \frac{1}{C_a n^2} \tag{3.8}$$

where C_a is the Auger capture probability coefficient and n is the free carrier density.

SRH recombination is an indirect process of electron-hole recombination, however there is an intermediate step that involves a trap produced by an impurity or a crystal dislocation. The trap acts as a recombination center where it captures the electron in a localized energy state in the bandgap before it can recombine with a hole. The energy is converted to a phonon. If a hole is also captured in the same recombination center, the electron-hole pair can be annihilated. If this does not occur, eventually the electron will decay down to the valence band to recombine with a hole, releasing a phonon. The recombination lifetime for this process is described by the SRH equation [4]:

$$\tau_{SRH} = \frac{\tau_{n0}(p_0 + p_1 + n) + \tau_{p0}(n_0 + n_1 + n)}{p_0 + n_0 + n} \tag{3.9}$$

where τ_{n0} and τ_{p0} are the capture time constants for electrons and holes respectively, p_0 and n_0 are equilibrium carrier densities for electrons and holes respectively, n_1 and p_1 are the equilibrium densities for electrons and holes when the Fermi level is equal to the defect energy level, respectively and n is the excess carrier density. The capture time constants can be determined using the defect concentration N_t, the capture cross-sections for electrons and holes σ_n and σ_p and the thermal capture velocity v_{th}. The relations are given as [4]:

$$\tau_{n0} = \frac{1}{N_t \sigma_n v_{th}} \tag{3.10}$$

$$\tau_{p0} = \frac{1}{N_t \sigma_p v_{th}} \tag{3.11}$$

SRH recombination lifetime measurements are useful for gauging the impurity levels in semiconductors. Defects cause harm in semiconductors so accounting for this can help improve the performance of devices.

As we can see from the processes that make up the bulk recombination, the effective lifetime is highly dependent on the concentration of excess carriers. In silicon, typical lifetimes can range from 1 μs to 1 ms. At low excess carrier concentrations, the recombination lifetime is primarily due to SRH. The lifetime also depends on the type of traps present in the material. Shallow traps reside near the edges of the bands resulting in short lifetimes, but deep traps lead to a lower probability of electrons escaping causing less recombination and therefore longer lifetimes. At high excess carrier concentrations, Auger recombination is dominant causing the lifetime to drop. For photovoltaics, longer lifetimes are favourable because they result in a higher probability for optically excited charge carriers to reach the pn-junction before they have a chance to recombine.

For silicon, the surface of a wafer contains many dangling bonds due to the abrupt discontinuity in crystal structure at the surface. Dangling bonds are unsatisfied valence states which act as traps for free carriers to recombine, reducing the overall number of dangling bonds. Unlike in SRH recombination where the trap energy levels are discrete, the trap energy levels for surface recombination are at a range of energy levels that can be related through its surface recombination velocity s as shown below [36]:

$$D\frac{dn}{dx} = -sn \tag{3.12}$$

where D is the diffusion coefficient and n is the excess carrier density.

High surface recombination can lead to carrier diffusion towards the surface if the bulk recombination rates are slower. This produces a flood of carriers at the surface, draining the bulk of free carriers. This makes it hard for bulk lifetimes to be measured especially in indirect semiconductors where the diffusion lengths can be quite large. The diffusion length describes the average distance free carriers can travel before they recombine. The surface lifetime is given by [36]:

$$\frac{1}{\tau_s} = \frac{1}{d(\frac{1}{2s} + \frac{d}{D\pi^2})} \tag{3.13}$$

where d is the wafer thickness.

3.3 Measurement of Lifetime in MFCA

In this section, the theory used to determine the recombination lifetime will be presented for MFCA (frequency domain). The theoretical equations and the derivations can be found in detail in Boyd's work [6]. A brief overview of his work will be described here.

The differential equation that describes the rate of change of free carriers (electrons or holes) in a semiconductor over time is given by [6]:

$$\frac{\partial n}{\partial t} = g(t) - \frac{n}{\tau_b} \tag{3.14}$$

where n is the excess carrier concentration, τ_b is the bulk recombination lifetime and $g(t)$ is the volumetric generation rate of free carriers. From looking at this equation we can see that the net rate of change of excess carriers is equal to the generation rate minus the recombination rate. For lifetime MFCA measurements, n can be experimentally found and $g(t)$ depends on the optical excitation method. The determination of $g(t)$ relies on the mode the experiment takes place (time, frequency, and quasi-steady-state domains).

In MFCA, the generation rate resembles a harmonically varying excitation with an angular frequency ω. This results in a harmonically varying n at the same frequency. The complex amplitudes for the generation rate and free carrier concentration can be written as $G(\omega)$ and $N(\omega)$ which converts these qualities to a harmonic form as shown below [6]:

$$g(t) = G(\omega)e^{i\omega t} \tag{3.15}$$

$$n = N(\omega)e^{i\omega t} \tag{3.16}$$

By substituting equations (3.15) and (3.16) into (3.14) and rearranging $N(\omega)$ we arrive at the frequency response under harmonic excitation for the free carrier concentration [6]:

$$N(\omega) = \frac{G(\omega)\tau}{1 + i\omega\tau} \tag{3.17}$$

With the assumption of a generation rate that is independent of frequency, equation (3.17) represents a Lorentzian function that resembles the response of a 1st order low-pass filter where the recombination lifetime is the reciprocal of the roll-off frequency. The modulation frequency is swept along a range of values while the $N(\omega)$ is demodulated using a lock-in amplifier. The magnitude of equation (3.17) is then used to curve fit the plot with the experimentally determined $N(\omega)$ to extract the bulk recombination lifetime. This procedure assumes a slow surface recombination velocity ($S \leq 1000 \frac{cm}{s}$) such that any contribution from surface recombination is negligible [6]. Therefore, in this case, the bulk recombination lifetime is equivalent to the total effective lifetime.

3.4 Calculation of FCA Cross-section

In this section, a derivation of the equations used to experimentally determine the FCA cross-section σ_{FCA} using MFCA in a pump-probe setup will be presented. The derivation was originally shown by Boyd in his work [6] [22].

As light hits a wafer, it can either be reflected, transmitted, or absorbed. In a semiconductor, if the absorption coefficient is low, the transmitted light can bounce many times within the material, transmitting a portion of the light at each bounce. The light is attenuated by a factor of $e^{-\eta\beta}$ at each bounce. The absorption factor β considers band-to-band and FCA absorption and is given by:

$$\beta = \alpha W + \alpha_{FCA} W \tag{3.18}$$

where α and α_{FCA} are the band-to-band and average free-carrier absorption coefficients, respectively, and W is the wafer thickness. The factor $\eta = \sec\theta$ describes the increase in path length through the wafer due to a non-normal angle of propagation.

The total transmission can be determined by summing up the transmission from each ray, leading to a generalized equation for the m^{th} ray:

$$P_{t1} = P_o\left(T^2 e^{-\eta\beta}\right)$$

$$P_{t2} = P_o\left(T^2 R^2 e^{-3\eta\beta}\right)$$

$$P_{tm} = P_o\left(T^2R^{2(m-1)}e^{-(2m-1)\eta\beta}\right) \tag{3.19}$$

where P_o is the initial power and T and R are the transmission and reflectance coefficients.

By converting equation (3.19) to an infinite summation and using a geometric series conversion we can arrive at the total transmission P_t through the wafer of:

$$P_t = P_0\frac{T^2e^{-\eta\beta}}{1-R^2e^{-2\eta\beta}}\ . \tag{3.20}$$

By substitution equation (3.18) into (3.20) and, letting $\mathrm{A} = e^{-\eta\alpha W}$ and $\mathrm{x} = \eta\mathrm{W}\alpha_{\mathrm{FCA}}$, the total transmitted power becomes:

$$P_t = \frac{P_0\mathrm{T}^2\mathrm{A}\mathrm{e}^{-\mathrm{x}}}{1-R^2\mathrm{A}^2\mathrm{e}^{-2\mathrm{x}}} \tag{3.21}$$

Equation (3.21) can also be referred to as the DC amplitude of the FCA signal. To determine the AC amplitude of the modulated FCA in the small-signal limit, the derivative with respect to x can be calculated:

$$\mathrm{P}_{\mathrm{t,AC}} = \frac{\mathrm{dP_t}}{\mathrm{dx}}\Delta\mathrm{x} = -P_0T^2\mathrm{A}\frac{(1+R^2A^2)}{(1-R^2A^2)^2}\ \Delta\mathrm{x} \tag{3.22}$$

where $\Delta\mathrm{x} = \eta\mathrm{W}\alpha_{\mathrm{FCA}} = \eta\mathrm{W}\sigma_{\mathrm{FCA}}\Delta n_1$ and Δn_1 is the time-dependent excess carrier density. Equation (3.22) now becomes:

$$\mathrm{P}_{\mathrm{t,AC}} = -P_0T^2\mathrm{A}\frac{(1+R^2A^2)}{(1-R^2A^2)^2}\ \eta\mathrm{W}\sigma_{\mathrm{FCA}}\Delta n_1 \tag{3.23}$$

The signal can be normalized by dividing the AC part by the DC:

$$\mathrm{P}_{\mathrm{t,AC}}/P_{t,DC} = \frac{1}{\mathrm{e}^{-\mathrm{x}}}\frac{(1+R^2A^2)(1-R^2\mathrm{A}^2\mathrm{e}^{-2\mathrm{x}})}{(1-R^2A^2)^2}\ \eta\mathrm{W}\sigma_{\mathrm{FCA}}\Delta n_1 \tag{3.24}$$

For silicon in general $\mathrm{x} = \eta\mathrm{W}\alpha_{\mathrm{FCA}} << 1$ such that the exponential terms raised to the x in (3.24) approach 1.

For silicon at short wavelengths, α is large which results in $\mathrm{A} = e^{-\eta\alpha W} << 1$ therefore $R^2A^2 << 1$. At long wavelengths α is small which results in $\mathrm{A} = e^{-\eta\alpha W} \approx 1$. However, at

long wavelengths $R < 1$ meaning R^2<<1 therefore R^2A^2 <<1. As R^2A^2 <<1 for all wavelengths it is considered negligible. Equation (3.24) simplifies to:

$$\mathrm{P_{t,AC}}/P_{t,DC} = \eta \mathrm{W} \sigma_{\mathrm{FCA}} \Delta n_1 \tag{3.25}$$

Equation (3.25) shows that the normalized signal is proportional to the FCA cross-section without dependence on the wavelength or transmission properties. AC and DC components are both affected by band-to-band absorption by the same amount which results in the elimination of any band-to-band contributions.

The AC amplitude of the excess carrier density Δn_1 under harmonic excitation in a semiconductor is given by a Lorentzian function as shown in section 3.3:

$$\Delta n_1 = \frac{\mathrm{mG}\tau}{\sqrt{(1+\omega^2\tau^2)}} \tag{3.26}$$

where m is the modulation depth, G is the time-averaged volumetric generation rate of free carriers and ω is the angular frequency from the pump source and τ is the effective recombination lifetime. The generation rate is defined as:

$$G = \frac{2 f_a P_{0,pu} \lambda_{pu}}{W A_{pu} h c} \tag{3.27}$$

where f_a is the fraction of absorbed pump power. $P_{0,pu}$, λ_{pu} and A_{pu} are the pump's incident power, wavelength, and beam area, respectively.

Substituting equations (3.26) and (3.27) into (3.25) leads us to the result of determining the FCA cross-section σ_{FCA} using MFCA and experimental measured quantities:

$$\mathrm{P_{t,AC}}/P_{t,DC} = \eta \sigma_{\mathrm{FCA}} \frac{\tau}{\sqrt{(1+\omega^2\tau^2)}} \frac{2\mathrm{m} f_a P_{0,pu} \lambda_{pu}}{A_{pu} h c} \tag{3.28}$$

The fraction of absorbed pump power f_a can be measured experimentally using the reflected and transmitted measurements or calculated using:

$$f_a = 1 - e^{-\eta_{pu} \alpha_{pu} W} \tag{3.29}$$

4. Experimental

4.1 Overview

In this chapter, an experimental outline will be described in detail. It will consist of two sections that have been categorized into relative wavelengths: long (1100 nm-2500 nm) and short (935 nm-1000 nm). The final section will be a comparison between the two as well as to reported results found in literature which were outlined in chapter 2. Each individual wavelength section will contain descriptions of the optical setup separated into pump and probe branches as well as the experimental results.

For both long and short wavelengths, the experimental setup is a conventional pump-probe design but with varying components and beam paths. Components that may vary include the pump/probe sources, detectors, and their respective filters. The complete setup can perform experiments at both long and short wavelengths. The setup contains two possible pump lasers at 532 nm and 1064 nm as well as a probe beam emitting at 345 nm-2500 nm from an optical parametric oscillator (OPO) or at 675 nm-1100 nm from a Ti:Sapphire laser. Details on the lasers used will be discussed in the later sections.

The pump lasers of 532 nm and 1064 nm have photon energies of approximately 2.33 eV and 1.16 eV, respectively. These photon energies are higher than that of silicon's bandgap (1.12 eV) which makes them ideal for inter-band absorption and optical injection of carriers. The probe beams are required to be weakly absorbed relative to the pump beams to facilitate intra-band absorption. Intra-band absorption does not need to meet an energy threshold to occur whereas inter-band absorption does (energy of the bandgap). The short wavelengths (935 nm (1.33 eV) - 1000 nm (1.24 eV)) that can also contribute to inter-band absorption require a pump that can dominate the inter-band transitions. Therefore, the 532 nm (2.33 eV) source is paired to the short wavelengths due to its significantly higher absorption coefficient. The long wavelengths (1100 nm (1.12 eV) - 2500 nm (0.5 eV)) do not contribute to inter-band absorption allowing for the 1064 nm (1.16 eV) pump to be used.

The samples used vary in thickness due to silicon's reflective, transmission, and absorption properties with respect to the wavelength. From equation (3.29), we can see as the thickness

of the sample increases, the exponential term would approach zero resulting in the fraction of absorbed power to also increase and approach 100%. However, it is not usually the thickness of the sample that makes the exponential term approach zero, rather it is the absorption coefficient that varies drastically with wavelength. At short wavelengths, the absorption coefficient is large, therefore a high fraction of absorbed pump power and vice versa at long wavelengths. Since the pump remains at a single wavelength f_a remains constant throughout the experiment. A higher f_a results in the generation of more carriers and a higher FCA signal which means a thicker sample could be more beneficial.

However, this may not be the case. It is also worth considering the transmission effects on wavelength for silicon. For silicon, the transmission of light is relativity low at short wavelengths compared to longer ones. Since these experiments only use the probe signal as the main experimental quantity in a transmitted orientation, high transmission of part of the probe beam is also needed across the wavelength range. This means at short wavelengths the FCA signal is a lot less compared to long wavelengths as less is being transmitted to the detector.

A solution to this is to use a thinner sample at the short probe wavelengths. A thinner sample will lower the pump's f_a and therefore lower the FCA signal but in order to see any FCA signal from the probe, a portion must be transmitted to the detector. A thinner sample results in less absorption and therefore more transmission of the FCA signal from the probe, this can be seen by applying equation (3.29) to the probe beam. The lower limits of the probe wavelength depend on how thin the sample can get for a valid transmission at the detector but also a reasonable enough f_a from the pump to generate carriers for an FCA signal in the first place.

4.2 FCA Measurements for Long Wavelengths (1100 nm-2500 nm)

4.2.1 Experimental Setup

The experimental setup can be broken down and explained by individual pump and probe branches. The pump branch (red beam) is sourced by a Laser Quantum Opus laser that produces 1064 nm horizontally polarized light. The laser is water-cooled using a heatsink that maintains its temperature at 22°C. The laser has a maximum

power of 10 W however in this work only 2 W is used. Upon exiting the laser, the height of the beam is raised to approximately 3 inches using a periscope. This ensures the beam is at a suitable height to be compatible with all the optical components used in the setup. The light is guided into an Conoptics electro-optical modulator (EOM) using a pair of mirrors (M5, M6). The EOM is designed from a Lithium Tantalate

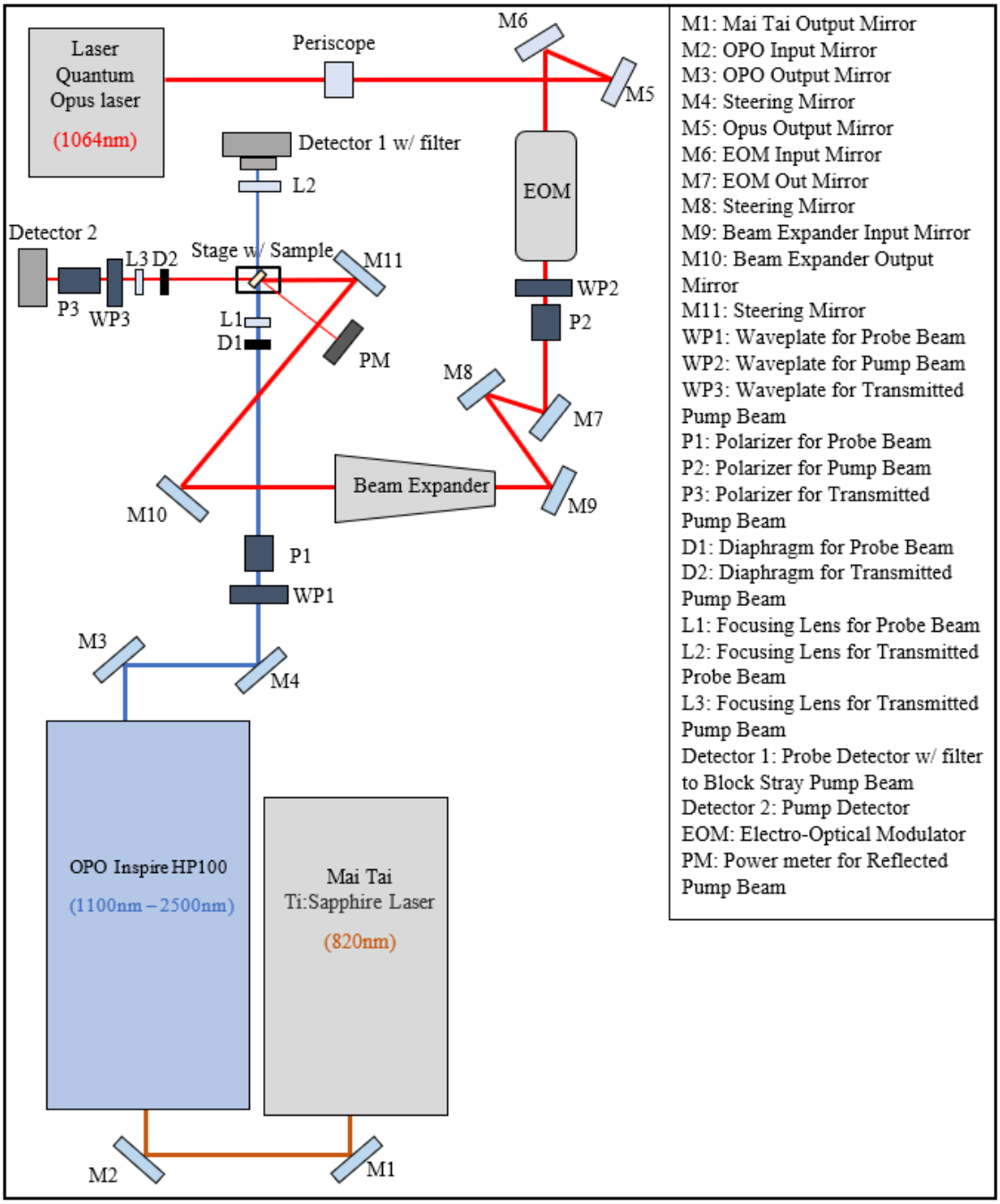

Figure 1: A graphical description for the optical layout of the long wavelength experiment.

Pockel's cell which is driven by a Conoptics Model 25 A driver. The driver induces an arbitrary analog signal on the laser beam that ranges from 0 to 25 MHz which provides the modulation for the pump beam. The modulation signal is produced by a Zurich Multi-Frequency lock-in amplifier in the form of a sinusoidal.

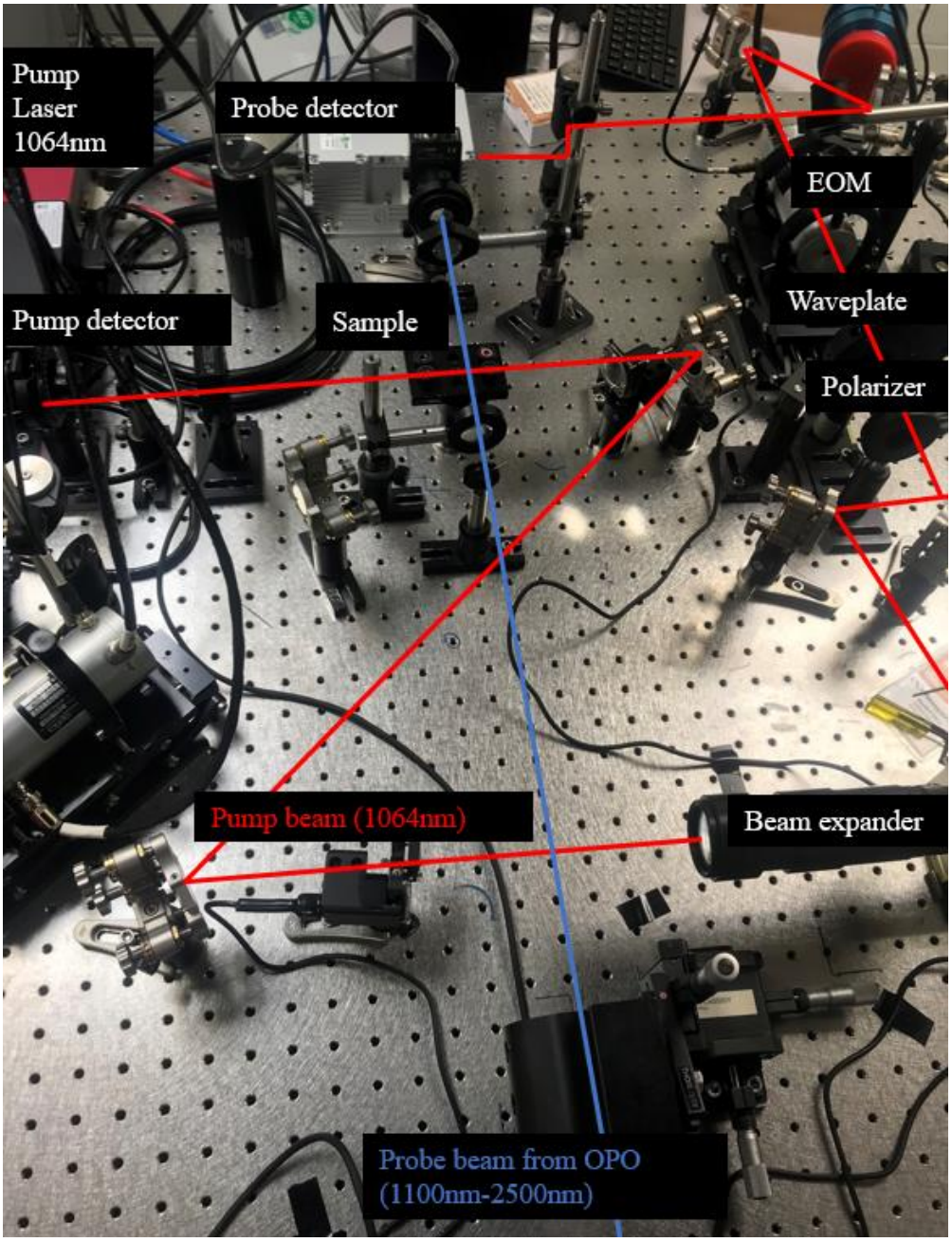

Figure 2: The optical table showing the layout of the long wavelength experiment.

The beam exits the output of the EOM into a half-waveplate and polarizer. By rotating the half-waveplate, the direction of polarization can be altered by changing the degree

of p- and s-polarization of the laser beam. Pairing the half-waveplate with a glan-laser calcite polarizer which only permits p-polarization to transmit through allows for this pair of components to act as a power attenuator upon rotation of the waveplate. For this work, the pump beam is set to approximately 600 mW. The beam then passes through a series of mirrors (M7-M9) which couples the light into a Standa beam expander which can increase the beam diameter 2-12x the original diameter. For this work, the beam diameter is varied between 3-5 mm. The enlarged beam exits the beam expander and is guided to the sample stage using a pair of mirrors (M10, M11).

After the light transmits through the sample, it passes through a diaphragm for alignment purposes and a focusing lens which focuses the light on a photoreceiver detector (Detector 2). A half-waveplate and polarizer pair are placed before the detector to reduce the power to ensure the detector does not get saturated. The detector is a Newport 2033 large area Germanium (Ge) photoreceiver with a wavelength range of 800 nm-1750 nm. It has a saturation power of 10 mW. This detector is connected to an oscilloscope where the waveform of the pump can be observed and analyzed. A Gentec power meter (PM) can be placed before the half-waveplate and polarizer pair to measure the full transmitted pump power through the sample. Likewise, the Gentec power meter is also used to measure the incident and reflected pump power.

The probe beam originates from the Spectra-Physics Mai Tai Ti:Sapphire mode-locked laser which operates at a wavelength range of 690 nm-1040 nm, a pulse width of 80-100 femtoseconds, a repetition rate of 80 MHz, and an average power up to 2.9 W. The Mai Tai is used to pump the INSPIRE HP100 optical parametric oscillator (OPO). The OPO provides tuning UV to IR (345 nm – to 2500 nm) with high power output in the UV and visible regions. The device is fully controlled using a computer interface meaning no change of intracavity optics or crystals is required.

The operation of the OPO can be explained in two stages; the first stage is the second harmonic generation (SHG) and the second stage is the optical parametric generation (OPG). The first stage starts when the Mai Tai beam enters the OPO via a pair of mirrors (M1, M2). The Mai Tai beam is set at a single wavelength of 820 nm which is in the middle of its tunable range to allow for maximum average power (2.9W) which

also translates to the widest OPO wavelength range. As the light enters the first stage, SHG occurs when two pump photons from the Mai Tai form to create a single photon of twice the energy. SHG is possible through the exploitation of nonlinear optics in crystalline materials. By rotating the nonlinear crystal through angle tuning it is

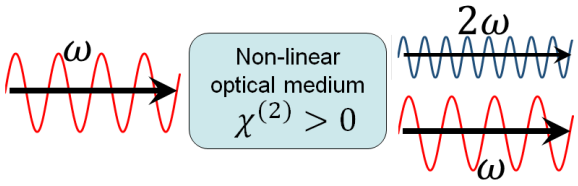

Figure 3: A visual showing the SHG process [41]. Pump beam (red), SHG beam (blue).

possible to find the orientation of the crystal with respect to the pump beam that produces the second harmonic. The second harmonic beam has a frequency that doubles that of the pump laser. This also means the energy is doubled and the wavelength is halved to 410 nm. Residual light from the pump beam also passes through the crystal, but its power is significantly reduced in the process. The SHG beam is used to pump the second stage.

For the second stage, photons from the second harmonic beam are split up into two separate beams referred to as the signal and idler. The sum of the signal and idler energies equals the energy of the second harmonic pump beam. This results in the conservation of the total energy where the solution can have an infinite number of wavelength possibilities as shown in equation (4.1).

$$\frac{1}{\lambda_{pump}} = \frac{1}{\lambda_{signal}} + \frac{1}{\lambda_{idler}} \tag{4.1}$$

To make this possible, a nonlinear crystal is placed inside the optical cavity and angle tuned such that the signal beam can produce wavelengths in the range of 490 nm – 750 nm. The wavelength generated depends on the angle of the crystal relative to the incident beam. The default position is when the front surface of the crystal is perpendicular to the incident beam, this produces light with a wavelength of 560 nm. We can see from the equation above with a fixed pump of 410 nm and with the signal beam generating light between 490 nm - 750 nm, this results in the idler wavelength range of 930 nm - 2500 nm. This is the primary output used in this work which can

generate infrared light up to 300 mW but only 30 mW of incident optical power at this wavelength range is required for a strong FCA signal.

The IR light exits the OPO and is guided towards the main setup using a pair of mirrors (M3, M4). Mirror 3 is on a fixed track such that any of the outputs can be used from the OPO with just one sliding mirror. This proved to be useful during the alignment process where the visible light output was used to make it easier to set up the beam path towards the sample. As the OPO probe beam approaches the sample it passes through a half waveplate and polarizer for power adjustments, a diaphragm for alignment purposes, and a focusing lens that focuses the beam to a diameter of approximately 50 µm on the sample. The transmitted probe beam is collected by a focusing lens which focuses the light on a ThorLabs InGaAs Amplified photodetector with a wavelength range of 800 nm - 2600 nm. The InGaAs detector is fitted with a 1064 nm Razer Edge ultra-steep long-pass edge filter to ensure that any stray light (≤1064nm) from the pump does not enter the probe's detector. The AC and DC components of the InGaAs detector are read using the lock-in amplifier that sweeps through a modulation frequency between 100 Hz to 100 kHz. The amplitude and phase of the FCA signal are measured at every step in a series of 50 equal logarithmically sized steps. This maps out a curve that resembles a Lorentzian function.

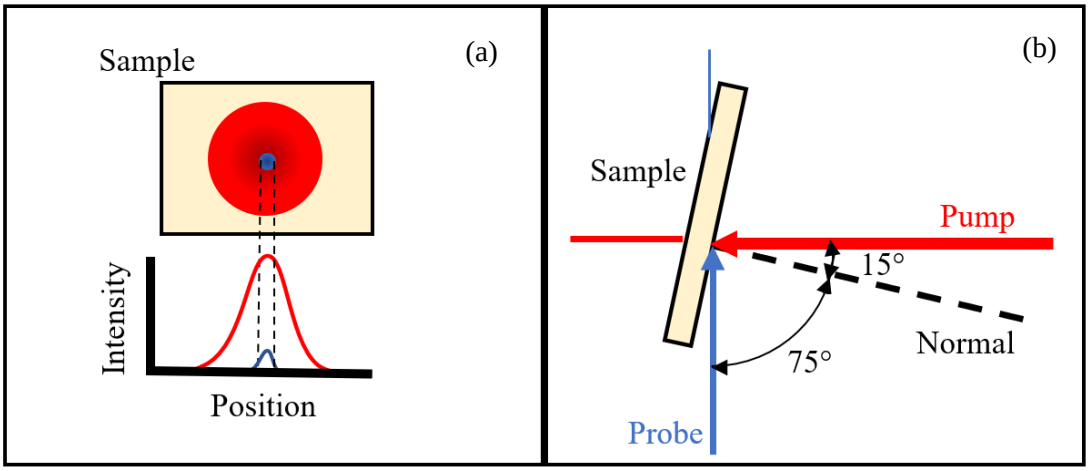

Figure 4: (a) The pump beam (red) can be considered constant over the area of probe beam (blue). (b) The orientation of the sample during experiments.

The sample used for the long wavelength experiment is a double-side polished silicon wafer with a native oxide present. The sample is lightly doped and is approximately

1.5 mm thick (See appendix B for further specifications). The sample is mounted on a rotating stage in the upright position. A benefit for the half waveplate/polarizer pair is that all the light hitting the sample is p-polarized meaning a Brewster angle exists for silicon at approximately 75°. Therefore to maximize the transmission, the angle of incidence for the probe beam is set to 75°. The angle of incidence for the pump beam is set to 15° as a result (Figure 4b).

Since both the pump and probe beams trace out a Gaussian beam profile as shown in Figure 4a, similar sized beam diameters would result in a non-uniform excess carrier concentration and a varying lifetime. To ensure this is not the case, the probe beam is made much smaller (50 μm) than the pump beam (3 mm) such that the pump beam can be considered constant over the area of the probe. Therefore, the measurements made by the probe are in a uniformly injected region resulting in a spatially uniform excess carrier concentration with a constant effective lifetime. Beam profiles are measured using the Nanoscan beam profiler in which their Gaussian distributions are confirmed.

4.2.2 Results

The data collection process is controlled using an Application Programming Interface (API) written in the Python programming language by Boyd. Minor adjustments had been made by Khabibrakhmanov and me to better suit our type of experiments. The API allows for control of the modulation frequency sweep range and the demodulation time constant which dictates the acquisition times. The time constant for the long wavelength experiments is set to 100 ms which produces clean decay curves. However, when the signal is weak as in the case of the shorter wavelengths, increasing the time constant will suppress random noise resulting in a cleaner curve. A time constant of 100 ms translates to a total acquisition time of two and half minutes. Each data acquisition presented here is performed twice if not more to verify the result of the previous and to allow for a result that can be averaged out over a few different measurements. The OPO is controlled on a separate graphical user interface (GUI) where the signal beam's wavelength can be set, which in turn changes the wavelength of the idler beam. The power output and stability of the OPO tend to degrade as the idler beam increases in wavelength.

A set of 4 data acquisitions can be seen below all measured at 1700 nm one after another. Each acquisition takes approximately two and half minutes resulting in a total of ten minutes to determine a reliable averaged AC amplitude and lifetime at that wavelength.

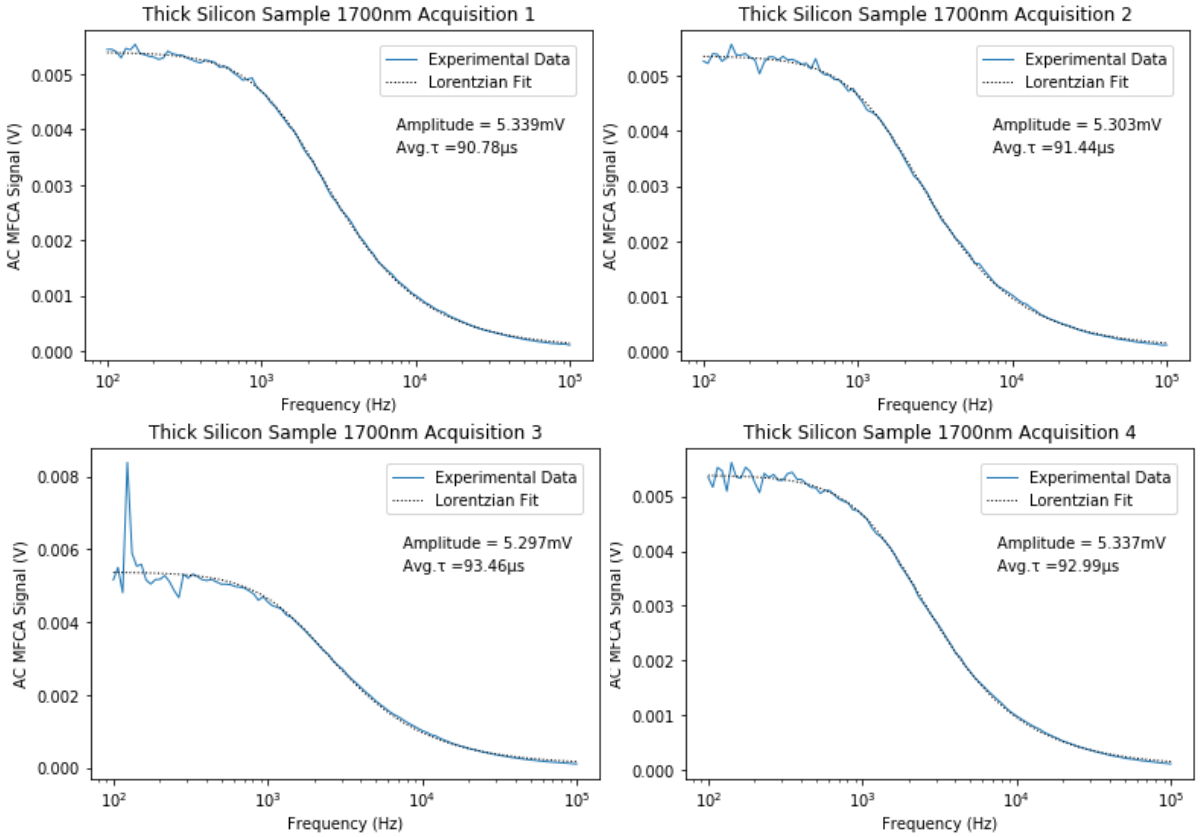

Figure 5: A set of 4 data acquisitions all measured at 1700 nm.

We can see at low frequencies the curves are subjected to random and background noise which is common for these experiments. However, this is not a problem as curve fitting ignores any outliers as seen in acquisition 3. The slight variations in the amplitudes and resulting lifetimes come from the stability of the probe beam. The probe beam has been seen to be inconsistent at times, shifting in powers from ±1-3 mW at random times. This ultimately comes down to the overall stability of the OPO. The OPO is very sensitive to temperature/humidity changes and even slight movement or touching of the OPO system can cause stability issues.

The measurements were taken from 1100 nm to 2500 nm in 100 nm steps with four acquisitions taken and averaged for each step. The results can be summarized in the table below:

Wavelength (nm)	AC Amplitude (mV)	DC Amplitude w/ offset (V)	DC Amplitude w/o offset (V)	Effective Lifetime (μs)
1100 ± 5	5.07 ± 0.01	4.60 ± 0.05	4.35 ± 0.05	85.30 ± 1.40
1200 ± 5	5.30 ± 0.01	3.90 ± 0.03	3.65 ± 0.03	93.26 ± 4.69
1300 ± 5	5.39 ± 0.01	3.66 ± 0.02	3.41 ± 0.02	97.72 ± 2.24
1400 ± 5	5.32 ± 0.01	3.08 ± 0.02	2.83 ± 0.02	95.10 ± 1.17
1500 ± 5	5.26 ± 0.01	2.50 ± 0.02	2.25 ± 0.02	96.20 ± 1.51
1600 ± 5	5.15 ± 0.02	2.02 ± 0.02	1.77 ± 0.02	98.62 ± 1.11
1700 ± 5	5.34 ± 0.01	1.81 ± 0.01	1.56 ± 0.01	92.17 ± 0.96
1800 ± 5	5.30 ± 0.02	1.60 ± 0.02	1.35 ± 0.02	96.33 ± 2.04
1900 ± 5	4.17 ± 0.01	1.16 ± 0.01	0.91 ± 0.01	94.67 ± 0.95
2000 ± 5	3.78 ± 0.01	0.98 ± 0.01	0.73 ± 0.01	95.80 ± 0.78
2100 ± 5	1.69 ± 0.01	0.55 ± 0.01	0.30 ± 0.01	98.63 ± 1.56
2200 ± 5	1.31 ± 0.01	0.47 ± 0.01	0.22 ± 0.01	96.89 ± 1.29
2300 ± 5	0.68 ± 0.01	0.35 ± 0.01	0.102 ± 0.009	94.34 ± 1.30
2400 ± 5	0.29 ± 0.01	0.29 ± 0.01	0.039 ± 0.008	97.67 ± 1.71
2500 ± 5	0.14 ± 0.01	0.27 ± 0.01	0.016 ± 0.005	91.43 ± 2.30
			Average Lifetime:	**95.01 ± 1.67**

Table 1: Measurements recorded from the Probe detector and Lorentzian curve fits.

Since the lifetime is assumed to be constant and does not depend on wavelength, the lifetimes are averaged out over the wavelength range to get a value of 95.01 ± 1.67 μs. This value will be the effective lifetime used to calculate future FCA values. At this point it is worth looking at equation (3.28) from chapter 3:

$$\frac{\mathrm{P_{t,AC}}}{P_{t,DC}} = s = \eta\sigma_{\mathrm{FCA}}\frac{\tau}{\sqrt{(1+\omega^2\tau^2)}}\frac{2\mathrm{m}f_a P_{0,pu}\lambda_{pu}}{A_{pu}hc} \qquad (3.28)$$

The next step is to determine the normalized signal s which can be calculated by dividing the AC power by the DC power. Equation (3.28) is represented in power measurements however by normalizing, the voltage values found from the Lorentzian fits can be used to determine s.

The decay curves and their associated Lorentzian fit at each wavelength can be plotted on the same graph to see the wavelength dependence on s. This is shown below:

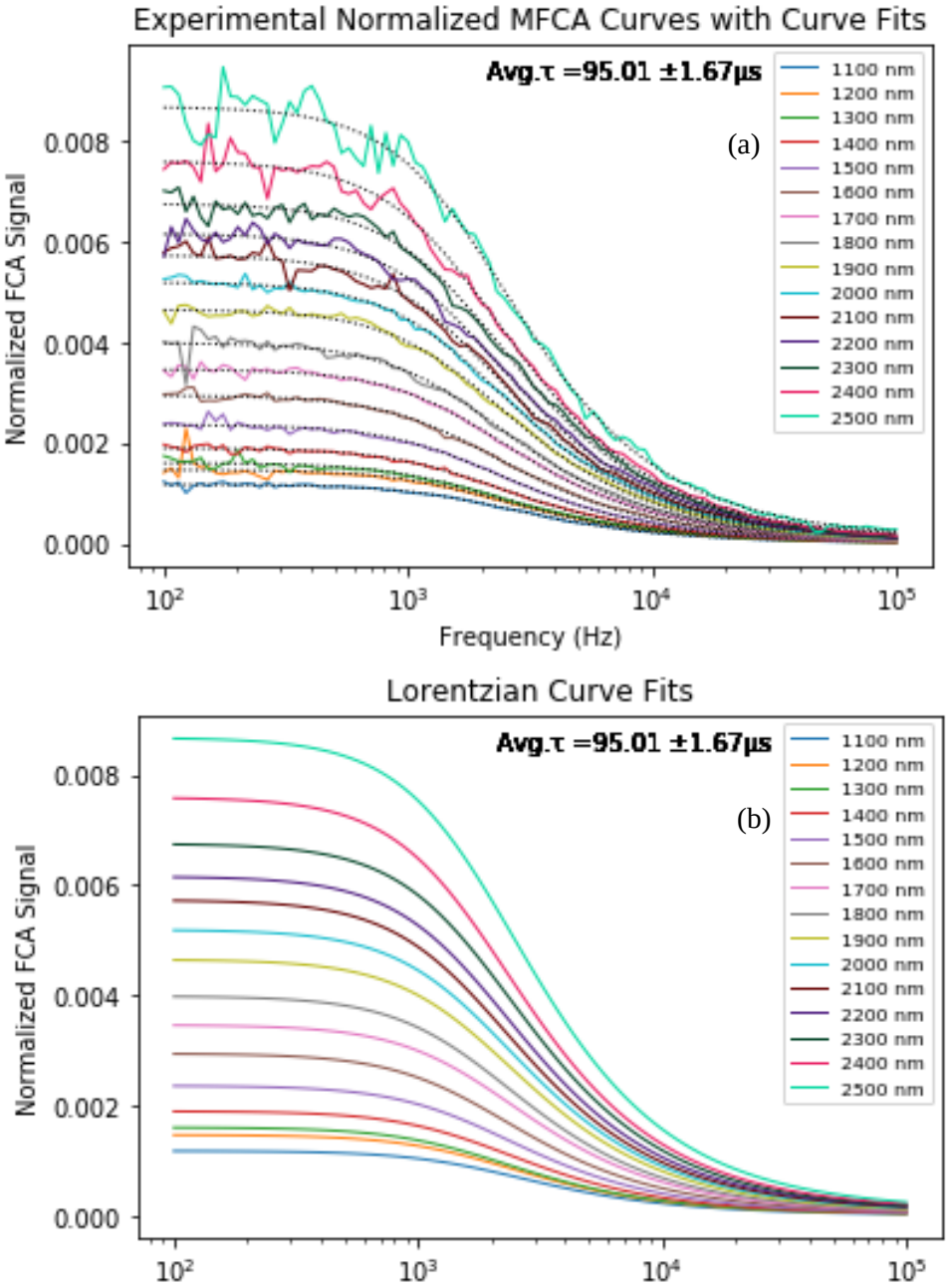

Figure 6:(a) Experimental Normalized MFCA and their associated curve fits. (b) The Lorentzian curve fits by themselves.

These graphs show that as the wavelength increases, the normalized FCA signal also increases. The spacing between each curve hints at a somewhat parabolic relationship, which is expected. If the spacing was equal between each curve it would suggest a linear relationship. The values of s at their associated wavelength can be plotted to reveal the true trend:

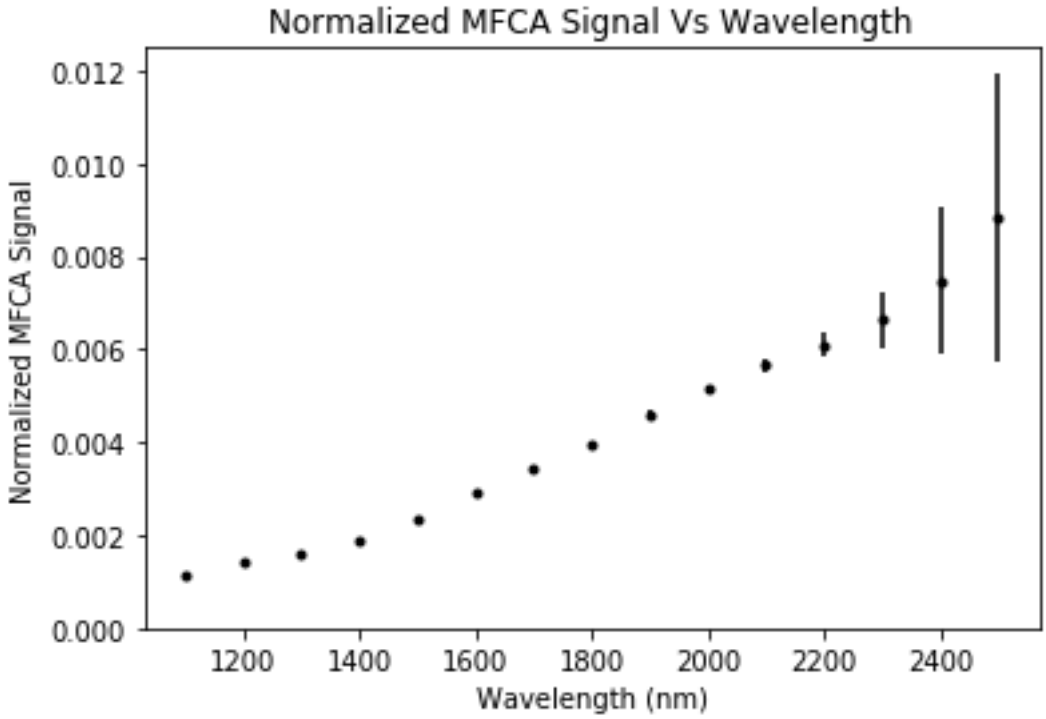

Figure 7: The normalized MFCA signal plotted against the full long wavelength range.

The graph resembles a parabolic trend. The error increases with wavelength because the error becomes more pronounced at small signal values. Small AC/DC signals result in larger normalized signals. When using the values from Table 1 to calculate s, a DC offset of 0.25V from the ThorLabs InGaAs Amplified photodetector has been considered. The offset was confirmed by performing a 'dark' test where measurements were recorded when there was no incident light on the detector.

To determine the σ_{FCA} at each wavelength we can rearrange equation (3.28) to solve for the cross-section. This essentially will be multiplying the normalized signal by material and universal constants. The trend should remain the same as Figure 7. The rearranged equation (3.28) turns into equation (4.2) as shown below:

$$\sigma_{\mathrm{FCA}} = \frac{s}{2\eta \mathrm{m} f_a P_{0,pu} \lambda_{pu} \tau} A_{pu} hc \tag{4.2}$$

The $\sqrt{(1+\omega^2\tau^2)}$ term in equation (3.28) can be neglected as we use the value for $\omega^2\tau^2 \ll 1$ from the fit, resulting in the term being equal to 1. The normalized signal s and the effective lifetime τ have been experimentally found as shown in Table 1 and Figure 7, respectively. The area of the pump A_{pu} is also experimentally found using the Nanoscan beam profiler. The fraction of the absorbed pump f_a was calculated by measuring the incident pump power $P_{0,pu}$ and reflected/transmitted powers on the Gentec power meter. The modulation depth m was calculated by analyzing modulation amplitude and mean power of the modulated pump signal from the Ge detector on the oscilloscope. The modulation depth is defined as half the peak-to-peak amplitude divided by the mean value[1]. The value of $\eta = \sec\theta_t$ describes the probe's beam path through the wafer, where the angle of refraction θ_t inside the semiconductor at the

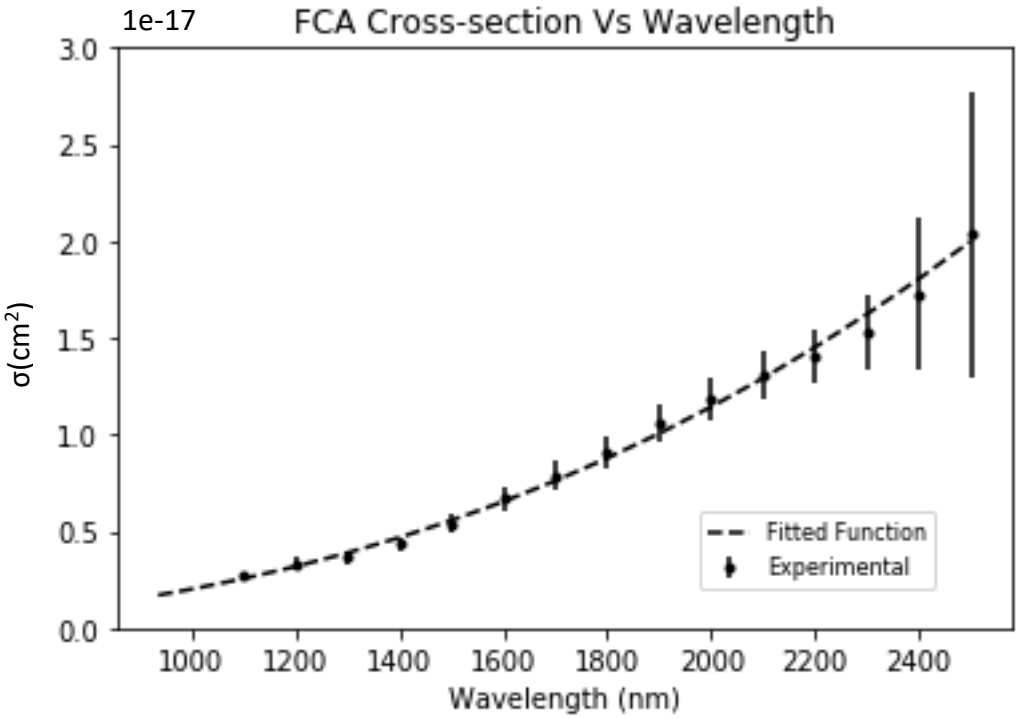

Figure 8: The calculated FCA cross-section plotted against the full long wavelength range.

[1] If measurements are recorded in RMS voltages a conversion must be made to peak values using, $m = \sqrt{2}\frac{V_{rms}}{V_{mean}}$. Measurements must stay consistent (either peak voltage or RMS) throughout the calculations or there could be a discrepancy of $\sqrt{2}$.

brewster angle is given by $\theta_t = \sqrt{1 + 1/n_r^2}$ where n_r is the index of refraction of the semiconductor. For silicon $n_r \approx 3.5$ and $\eta = 1.04$ [37].

The calculated σ_{FCA} values using equation (4.2) can be plotted vs. wavelength and are displayed in Figure 8. The error has increased due to uncertainty introduced in the experimentally measured constants. The plot can be fitted using equation (3.4) from chapter 3:

$$\sigma_{FCA} = C_{FCA}\lambda^{\xi} \tag{3.4}$$

Using python's built-in optimize.curve.fit() function with initial guesses of $C_{FCA} = 1$ and $\xi = 2$, and original error bars, equation (3.4) is parameterized into:

$$\sigma_{FCA} = (2.09 \times 10^{-8} \pm 1.05 \times 10^{-8})\, \lambda^{2.50 \pm 0.06} \tag{4.3}$$

Equation (4.3) is in units of cm for the wavelength and cm^2 for σ_{FCA}.

The FCA coefficient can be determined now by using equations (3.2, 3.26, and 3. 27) presented in chapter 3.

$$\alpha_{FCA} = \sigma_{FCA}\Delta n_0 \tag{3.2}$$

$$\Delta n_1 = \frac{\mathrm{mG\tau}}{\sqrt{(1 + \omega^2\tau^2)}} \tag{3.26}$$

$$G = \frac{2 f_a P_{0,pu} \lambda_{pu}}{W A_{pu} h c} \tag{3.27}$$

The magnitude of the AC amplitude of the excess carrier density Δn_1 can be related to the mean excess carrier density Δn_0 induced by the pump through the modulation depth m.

$$\Delta n_0 = \frac{\Delta n_1}{m} = G\tau = \frac{2 f_a P_{0,pu} \lambda_{pu}}{W A_{pu} h c}\,\tau \tag{4.4}$$

Using equation (4.4) and the average effective lifetime calculated for this set of wavelengths, the mean excess carrier density Δn_0 induced by the pump is $1.74 \times 10^{16} \pm 1.58 \times 10^{15}\ cm^{-3}$. Using this Δn_0 value and the σ_{FCA} values from

equation (4.3), the FCA coefficient α_{FCA} can be calculated at each wavelength using equation (3.2). The plot of this is shown below:

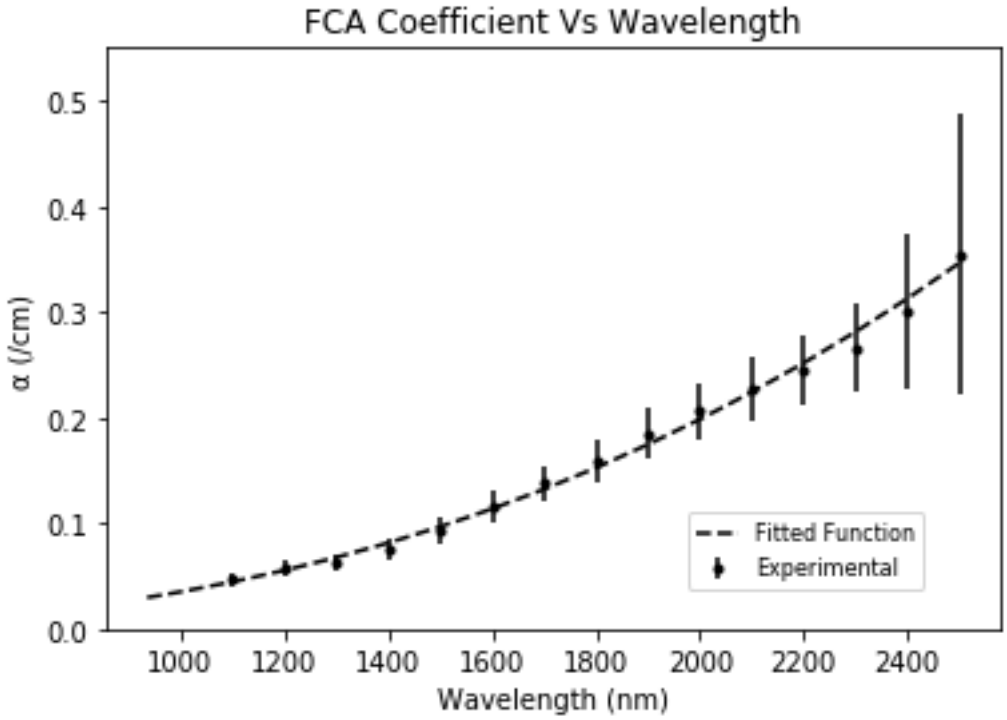

Figure 9: The calculated FCA coefficient plotted against the full long wavelength range.

As expected, the trend of the graph remains the same as the σ_{FCA} values are only multiplied by the constant Δn_0. The α_{FCA} values here are written in units of cm^{-1} as that is what it is commonly represented in. Using the fitting function (3.3) displayed in chapter 3, this graph can be fitted to it:

$$\alpha_{FCA} = C_{FCA}\lambda^{\xi}\Delta n_0 \tag{3.3}$$

Once again, using python's built-in optimize.curve.fit() function with initial guesses of $C_{FCA}\Delta n_0 = 1 \times 10^8\ cm^{-3}$ and $\xi = 2$, and original error bars equation (3.3) is parameterized into equation (4.5):

$$\alpha_{FCA} = (3.38 \times 10^8 \pm 1.65 \times 10^8)\ \lambda^{2.50\pm0.06} \tag{4.5}$$

To find C_{FCA}:

$$C_{FCA}\Delta n_0 = 3.38 \times 10^8 \rightarrow \ C_{FCA} = \frac{3.38 \times 10^8 cm^{-3}}{1.74 \times 10^{16}\ cm^{-3}} = 1.94 \times 10^{-8}$$

Therefore, the final equation (4.6) that relates α_{FCA} $[cm^{-1}]$ to any wavelength $[cm]$ and to any arbitrary excess carrier concentration $[cm^{-3}]$ is:

$$\alpha_{FCA} = (1.94 \times 10^{-8} \pm 7.37 \times 10^{-9})\ \lambda^{2.50 \pm 0.06} \Delta n_0 \tag{4.6}$$

Equation (4.6) is only valid within the experimentally measured wavelength range of (1100 nm – 2500 nm).

4.3 FCA Measurements for Short Wavelengths (935 nm-1000 nm)

4.3.1 Experimental Setup

The experimental setup for the short wavelengths requires components to be added to the original setup (Figure 1). In the overview of this chapter, it was explained that a new pump source was needed such that the wavelength of the pump was lower than that of the probe.

The new pump is a continuous wave (CW) 532 nm laser from Laser Quantum capable of producing a maximum of 300 mW of optical power. A second electro-modulator (EOM) is also required, suitable for 532 nm. Another Conoptics EOM is used to modulate the pump beam. Due to the EOM model available, only approximately 76 mW is allowed to transmit through to the sample. This will affect the strength of the FCA signal as well as the other reasons mentioned in the overview obtaining a good signal at the short wavelength will prove to be difficult.

Due to complications with the OPO at the time, a new probe beam has also been introduced into the setup. The new probe is a Spectra-Physics 3900s CW Tunable Ti:Sapphire laser pumped by a Spectra-Physics Millennia eV high power CW laser at 532 nm with 5 mW of optical power. This translates to the 3900s being tunable from 675 nm to 1100 nm at a maximum optical power of 3.5 mW.

To incorporate these 2 additional lasers into the setup without removing the original lasers, a few modifications are required using flipper mirrors. Similar to that of the 1064 nm pump, the light exits from the 532 nm pump and hits a periscope which raises the beam to approximately 3 inches above the table. This ensures the beam is at a suitable height to be compatible with all the optical components used in the setup. The

light is guided into a Conoptics electro-optical modulator (EOM) using a single mirror (12). The EOM is designed from a potassium dideuterium phosphate Pockel's cell which is driven by a Conoptics Model 25 A driver. The driver induces an arbitrary analog signal on the laser beam that ranges from 0 to 25 MHz which provides the modulation for the pump beam. The modulation signal is produced by a Zurich Multi-Frequency lock-in amplifier in the form of a sinusoidal shape. This process is the same as for the 1064 nm pump.

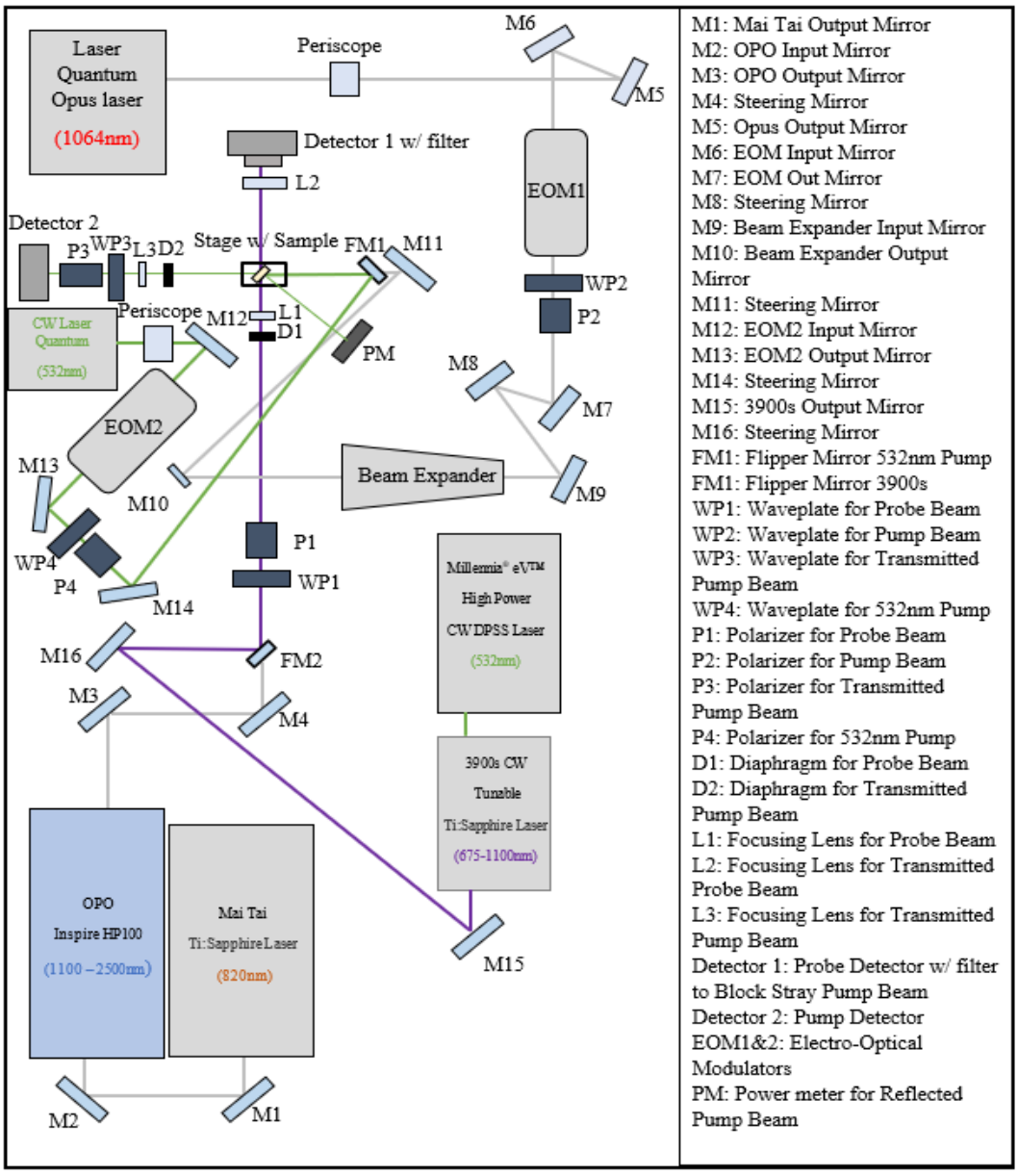

Figure 10: A graphical description for the optical layout of the long and short wavelength experiment.

The beam exits the output of the EOM and is guided into a half-waveplate and polarizer by a mirror (M13). The half-waveplate and polarizer combination act as a power attenuator upon rotation of the waveplate. A steering mirror (M14) guides the beam in the general direction of the sample. The beam hits a flipper mirror (FM1) which directs the beam onto the sample. The purpose of FM1 is that when it is in the down position the 1064 nm pump can be used normally. When FM1 is in the up position the 1064 nm would hit the back of it and be blocked. FM1 allows for both pump beams to be used in the same alignment given the orientation of it. This means the position of the sample and detector does not need to be changed. However, since the Ge 2033 detector does not detect 532 nm, a Newport silicon (Si) detector is used instead. The Si detector has a wavelength range of 190-1100 nm and a saturation power of 5 mW. This detector is connected to an oscilloscope to analyze the waveform of the pump beam when the sample is removed. The Gentec power meter (PM) is used to measure the incident and transmitted/reflected pump power from the sample.

The probe originates from Millennia eV 532 nm laser which pumps the Ti:Sapphire laser allowing it to emit in the ideal range of 675 nm – 1100 nm. The laser is controlled using a GUI on the computer where the wavelength can be set. Upon exiting the output of the 3900s, the beam is reflected off a mirror (M15) which sends the beam towards M16. Mirror M16 guides the light towards a flipper mirror (FM2) which directs the light towards the sample. It passes through a half-waveplate and polarizer combination before hitting the sample. The flipper mirror allows for the beams from the OPO to also be used in the same configuration when the flipper mirror is in the down position. The probe transmits through the sample where it is focused on a Ge 2033 detector outfitted with a filter to block stray 532 nm light. The AC and DC components of the Ge detector are read using the lock-in amplifier that sweeps through a modulation frequency from 100 Hz to 100 kHz. The amplitude and phase of the FCA signal are

measured at every step in a series of 50 equal logarithmically sized steps. This maps out a curve that resembles a Lorentzian function.

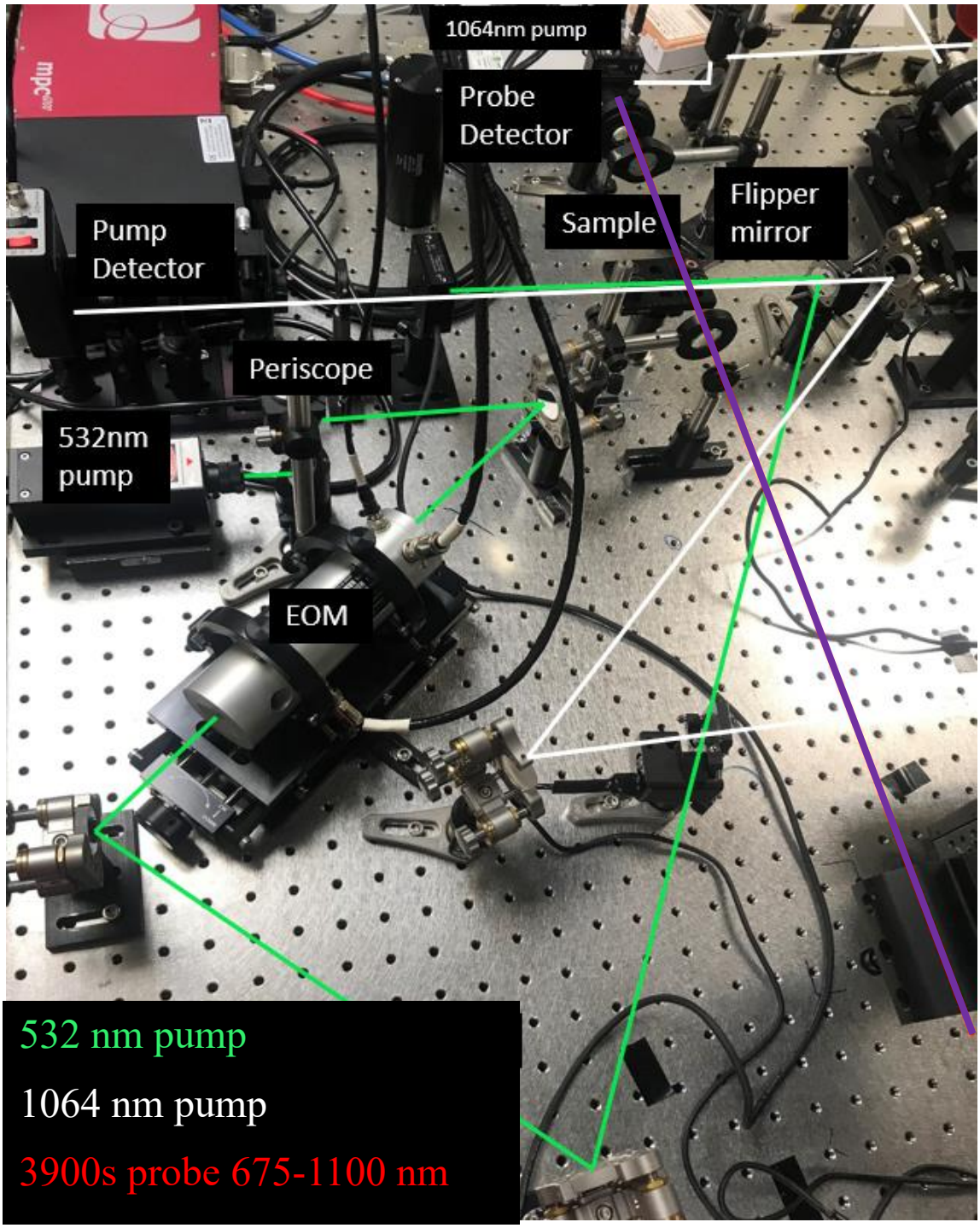

Figure 11: The optical table showing the layout of the short wavelength experiment.

The sample used for the short wavelength experiment is a double-side polished silicon wafer with a native oxide coating. The sample is lightly doped and is approximately 325 μm thick (See appendix B for further specifications). The sample is mounted as close as possible to the Brewster angle to maximize transmission. The probe beam remains smaller (50 μm) than the pump beam (5 mm) such that the pump beam can be considered constant over the area of the probe. Therefore, the measurements made by the probe are in a uniformly injected region resulting in a spatially uniform excess carrier concentration with a constant effective lifetime. Beam profiles are measured using the Nanoscan beam profiler in which their Gaussian distribution is verified.

4.3.2 Results

The data collection process for the short wavelengths is the same as explained in section 4.2.2. The wavelength tested are in the range of 935 nm - 1007 nm in step sizes of approximately 10 nm. The step sizes may vary a few nanometers due to how the 3900s laser wavelength selection is operated. A stepper motor is used to drive the birefringent filter assembly which determines the wavelength produced. The stepper motor was increased in equal step sizes of 5 mm which translated to the wavelength range presented here.

As mentioned in the overview of this chapter, the time constant on the lock-in's low pass filter has been increased to 400 ms for these experiments. A higher time constant will create a narrower bandwidth which will ultimately reduce noise and clean up the signal. This is important when the signal is low and plagued with noise as we will see in this wavelength range. This is due to the reduced FCA signal from a lower pump power and that at short wavelengths the FCA signal is reduced due to the lower transmission through the sample to the detector.

Increasing the time constant to 400 ms quadruples the acquisition time from approximately 2.5 minutes to 10 minutes. Doing so reduces noise significantly, improving the overall accuracy of the Lorentzian fit. This is shown below in Figure 12 with the probe set at 1000 nm.

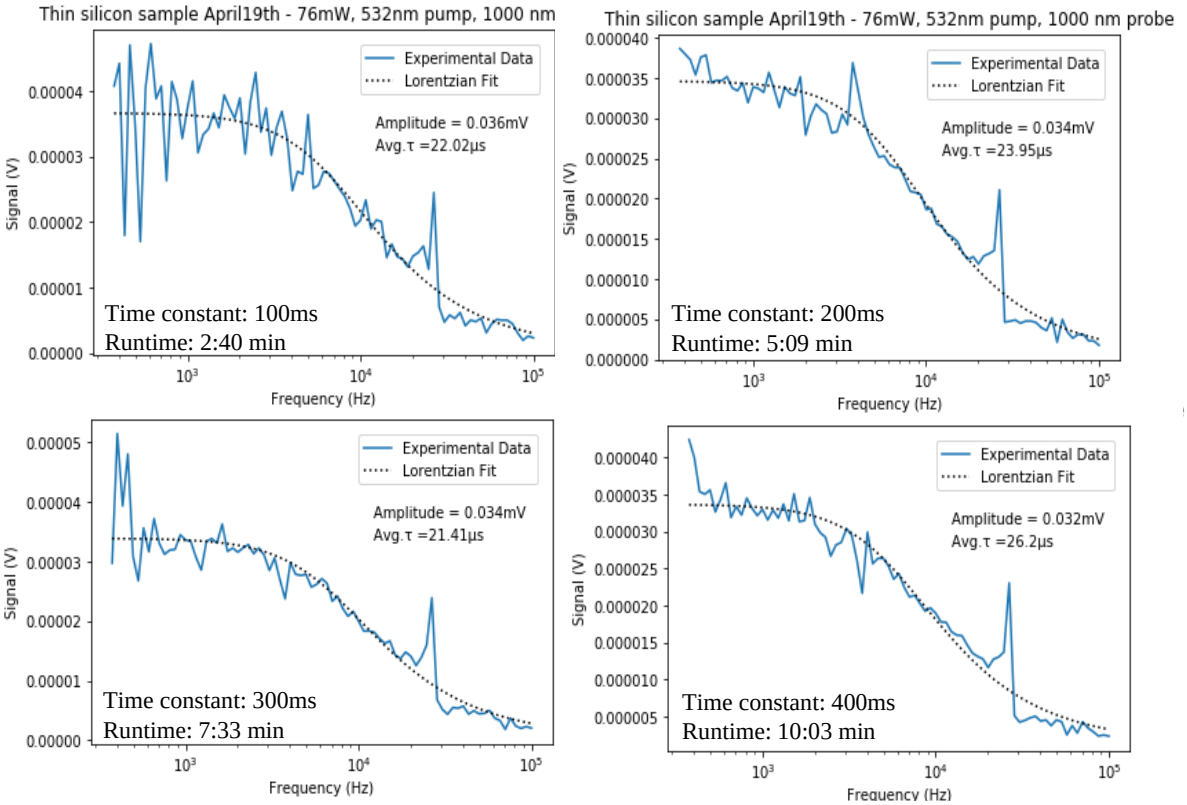

Figure 12: A set of 4 data acquisitions all measured at 1000 nm with different time constants. Data shown is for demonstration purposes only, not used in future calculations. See Appendix D.

Likewise, to the previous experiment, we can prepare a table that displays the wavelengths tested and their associated AC/DC components as well as an average effective lifetime for the sample. The results can be summarized in the table below:

Wavelength (nm)	AC Amplitude (µV)	DC Amplitude (V)	Effective Lifetime (µs)
1007 ± 5	18.6 ± 1.3	0.590 ± 0.002	28.50 ± 2.87
1000 ± 5	13.2 ± 1.5	0.424 ± 0.002	31.84 ± 1.82
992 ± 5	10.1 ± 1.7	0.331 ± 0.002	35.47 ± 3.25
980 ± 5	8.6 ± 1.2	0.29 ± 0.01	30.64 ± 2.75
973 ± 5	6.4 ± 0.4	0.24 ± 0.01	35.82 ± 3.25
964 ± 5	4.3 ± 0.4	0.17 ± 0.01	27.51 ± 4.42
955 ± 5	5.2 ± 0.4	0.21 ± 0.01	31.72 ± 5.65
948 ± 5	4.3 ± 0.4	0.17 ± 0.01	26.96 ± 4.26
943 ± 5	4.4 ± 0.3	0.19 ± 0.01	30.73 ± 4.80
935 ± 5	2.9 ± 0.2	0.14 ± 0.01	37.75 ± 6.33
		Average Lifetime:	**31.70 ± 3.94**

Table 2: Measurements recorded from the Probe detector and Lorentzian curve fits.

Since the lifetime is assumed to be constant and does not depend on wavelength, the lifetimes are averaged out over the wavelength range to get a value of 31.70 ± 3.94 µs. This value will be the effective lifetime used to calculate future FCA values.

The next step is to use equation (3.28) to determine the normalized signal s which can be calculated by dividing the AC power by the DC power. Equation (3.28) is represented in power measurements; however by normalizing, the voltage values found from the detector and Lorentzian fit can be used to determine s.

The Lorentzian fit at each wavelength can be plotted on the same graph to see the wavelength dependence of s. This is shown below:

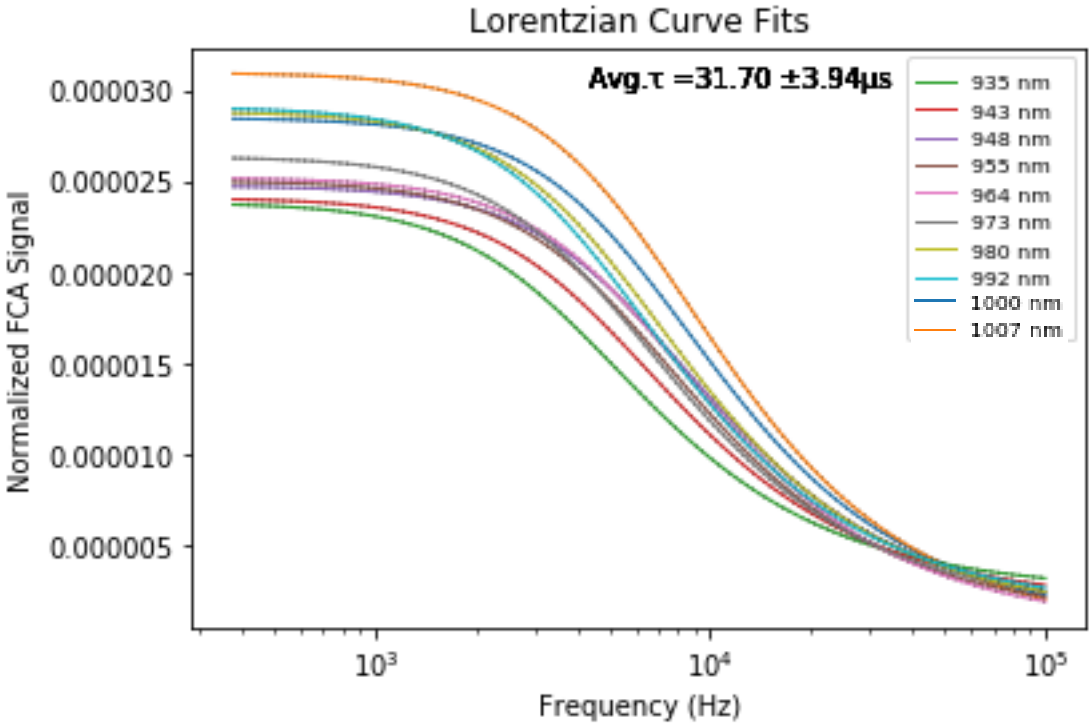

Figure 13: The normalized Lorentzian curve fits across the whole short wavelength range.

These graphs show that as the wavelength increases, the normalized FCA signal also increases. This trend does not hold entirely true for wavelengths in the range of 980 nm-1000 nm. At low-frequency values, the normalized signal for 980 nm and 992 nm is higher than the signal at 1000 nm. These three values are close together and have uncertainties associated with them that can account for the discrepancy. The spacing between each curve does not hint at any resemblance of a parabolic relationship.

However, when looking at the amplitudes of the curves, they all fall within a small range of 0.000023-0.000032 which makes it difficult to see the wavelength-dependent trend with these curves. Therefore, we can convert our normalized values to FCA cross-section values using equation (4.2) and plot vs wavelength to see how the trend is behaving. This is shown below in Figure 14:

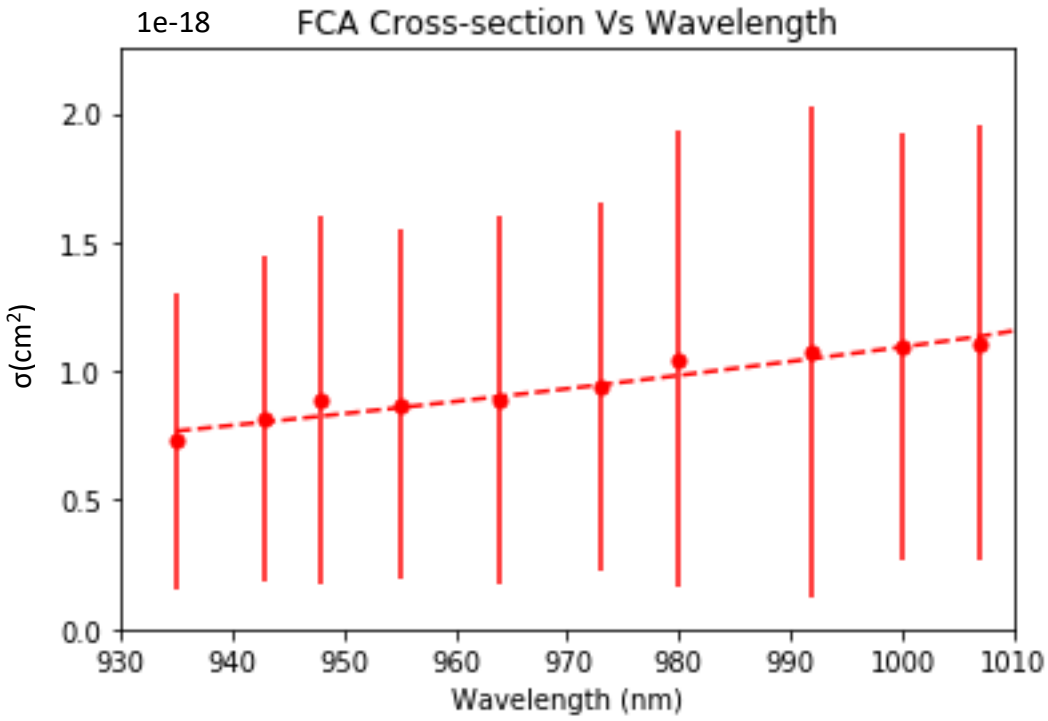

Figure 14: The calculated FCA cross-section plotted against the full short wavelength range.

At first inspection, it may look linear however since it's over a small wavelength range of 935 nm to 1007 nm, it could frankly represent something else.

Using python's built-in optimize.curve.fit() function with initial guesses of $C_{FCA} = 1$ and $\xi = 2$ and original error bars, equation (3.4) is parameterized into equation (4.7):

$$\sigma_{FCA} = (1.26 \times 10^3 \pm 5.80 \times 10^2)\, \lambda^{5.27 \pm 0.50} \qquad (4.7)$$

Equation (4.7) is in units of cm for the wavelength and cm^2 for σ_{FCA}.

The mean excess carrier density Δn_0 can be calculated using equation (4.4). Comparing to the previous experiment with long wavelengths, the fraction of absorbed pump power f_a has increased due to a strong absorption coefficient at 532 nm, the incident pump power has decreased and is limited by the laser and EOM to just 76

mW. The pump wavelength λ_{pu} and the effective lifetime has decreased. The thickness of the wafer W has decreased and the area of the pump beam A_{pu} has remained the same. This ultimately leads to a decrease in Δn_0 by almost an order of magnitude, which is another main reason for the low FCA signal; a lack of free carriers in the conduction band.

$$\Delta n_0 = \frac{\Delta n_1}{m} = G\tau = \frac{2 f_a P_{0,pu} \lambda_{pu}}{W A_{pu} hc}\tau = 5.06 \times 10^{15} \pm 1.28 \times 10^{15}\ cm^{-3}$$

Using this Δn_0 value and the σ_{FCA} values from equation (4.7), the FCA coefficient α_{FCA} can be calculated at each wavelength using equation (3.2). The plot of this is shown below:

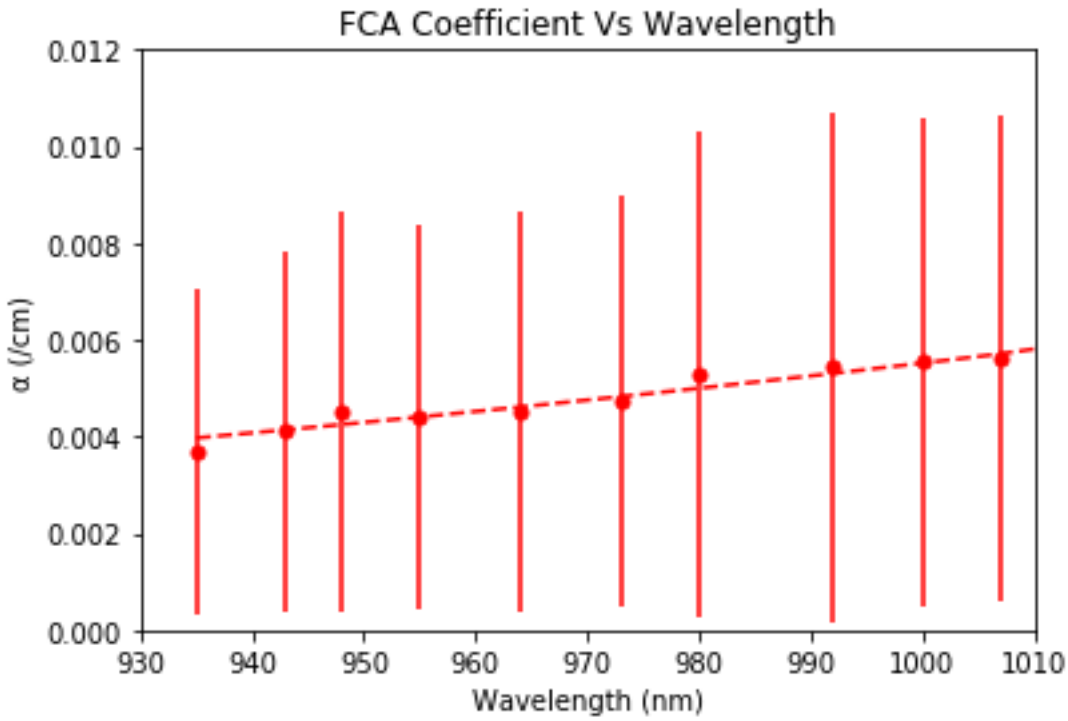

Figure 15: The calculated FCA coefficient plotted against the full short wavelength range.

As expected, the trend of the graph remains the same as the σ_{FCA} values are only multiplied by the constant Δn_0. The α_{FCA} values here are written in units of cm^{-1} as that is what it is commonly represented it. Using the fitting function (3.3) displayed in chapter 3, this graph can be fitted to it:

$$\alpha_{FCA} = C_{FCA} \lambda^{\xi} \Delta n_0 \tag{3.3}$$

Once again, using python's built-in optimize.curve.fit() function with initial guesses of $C_{FCA}\Delta n_0 = 1 \times 10^{15}\ cm^{-3}$ and $\xi = 2$, equation (3.4) is parameterized into equation (4.8):

$$\alpha_{FCA} = (2.15 \times 10^{17} \pm 9.94 \times 10^{16})\ \lambda^{4.90\pm0.50} \tag{4.8}$$

To find C_{FCA}:

$$C_{FCA}\Delta n_0 = 2.15 \times 10^{17}\ cm^{-3} \rightarrow\ C_{FCA} = \frac{2.15 \times 10^{17}\ cm^{-3}}{5.06 \times 10^{15} cm^{-3}} = 42.5 \pm 22.4$$

Therefore, the final equation (4.9) that relates α_{FCA} $[cm^{-1}]$ to any wavelength $[cm]$ and to any arbitrary excess carrier concentration $[cm^{-3}]$ is:

$$\alpha_{FCA} = (42.5 \pm 22.4)\ \lambda^{4.90\pm0.50}\Delta n_0 \tag{4.9}$$

Equation (4.9) is only valid within the experimentally measured wavelength range of (935 nm – 1007 nm).

4.4 Comparison at all Wavelength and with Literature

The first comparison we can make is between the parameterized equations (4.6 and 4.9) derived from the long and short wavelength experiments. To keep the equations consistent with each other the value for the excess carrier concentration Δn_0 must be the same in both equations. Both equations should be valid for any arbitrary excess carrier concentration, however, to due large relative experimental uncertainties especially at the lower wavelengths and the fact that the equations have different ξ we expect there to be a large difference. Furthermore, a systematic error between the two datasets is highly possibly due to the number of variables that had been changed. We will try to predict this systematic error after we compared the original values.

The two Δn_0 values that were experimentally found will be used to compare the FCA coefficients. First though, we can compare the FCA cross-section σ_{FCA} as a Δn_0 is not required for that. The fitted curve for each parametrized equation will cover the whole wavelength range from 935 nm to 2500 nm. This will allow us to see how the curves compare to each other. Since the ξ value for the short wavelength equation is 5.27

compared to 2.50 for the long wavelength it will not be worth comparing the curves at a longer wavelength as $\xi = 5.27$ will cause the σ_{FCA} values to explode. This occurs at wavelengths past 1300 nm.

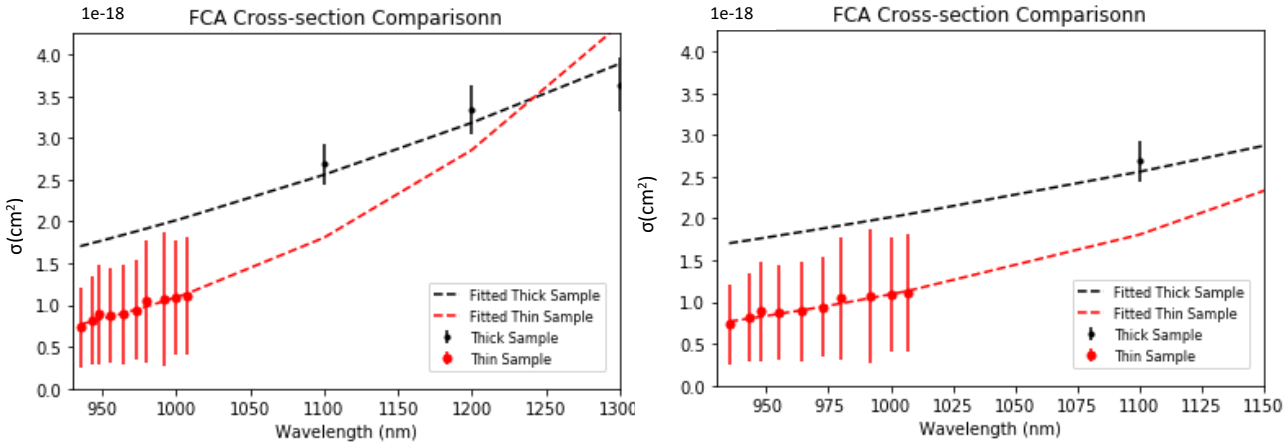

Figure 16: A comparison between the long and short wavelength cross-sections at (935-1350 nm) and (935-1150 nm).

In all cases, expect for an overlap at around 1250 nm, the points measured in the long wavelength (1100-2500 nm) experiment do not agree within their uncertainties when compared with the fitted short wavelength curve. This concludes that the parametrization equation (4.9) found for the short wavelengths is only potentially valid within the experimentally measured range of 935-1007 nm. More interestingly, the long wavelength parametrization equation (4.3) can be compared to the measured points at the at short wavelength range (Figure 13). We can see the experimentally measured points at the short wavelengths also do not agree with equation (4.3) within their uncertainties however it is much closer in this case. The resultant difference can be explained by unaccounted systematic errors developed between the two datasets since many variables had changed. Most noticeably would be the change of sample and pump beam. Between the two datasets, there is approximately a factor of 2 difference and if the short wavelength values were increased by roughly 40% the error bars on the measured points would fall within the parametrization equation (4.3). The overall trend within the 935-1007 nm range does appear to be common among the two curves.

To compare the FCA coefficients, equations (4.3) and (4.7) must get multiplied by the same experimentally found Δn_0. We can expect somewhat of the same behaviour and

validation as α_{FCA} is just scaled by Δn_0. We also do expect slight differences in the curve fits as they consider the error bars which naturally grow over time and are different between two Δn_0 values. The introduction of the error in Δn_0 increases the overall error which changes the curve fit and the associated parametrization. We can see below in Figure 17, this increase has allowed a few of the error bars to lie within the parameterization equation for the long wavelengths when $\Delta n_0 = 5.06 \times 10^{15} cm^{-3}$. This is because $\Delta n_0 = 5.06 \times 10^{15} cm^{-3}$ has a higher error tied to it. Assuming a systematic error is present between the two datasets, a correction factor of approximately 30% is required to make all error bars fall within the parameterization equation for the long wavelengths at both Δn_0 values. Also, at both Δn_0's the measured values at the short wavelengths are different by a factor of approximately 2 when compared to the parameterization at the long wavelengths. The overall trend within the 935-1007 nm range remains the same and is still common among the two fitted curves.

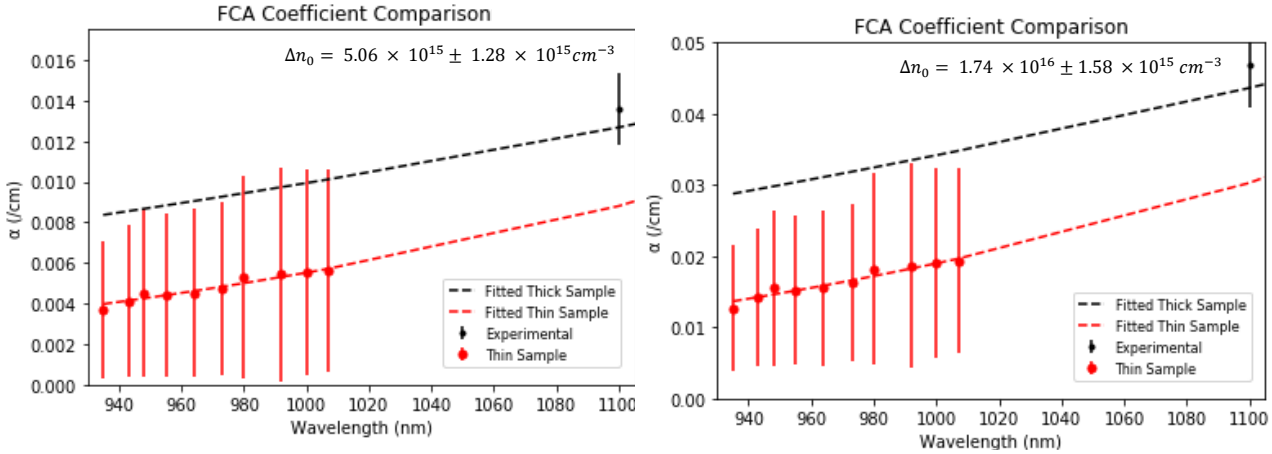

Figure 17: A comparison between the long and short FCA coefficients at two different experimentally found Δn_0 values.

Next, we can compare the FCA coefficient, α_{FCA} for the optical methods. This includes work from Svantesson, Meitzer, Boyd, Khabibrakhmanov, Gauster and Linnros. To compare, we use the experimentally calculated Δn_0 from this work which is $1.74 \times 10^{16} \pm 1.58 \times 10^{15} cm^{-3}$ or $5.06 \times 10^{15} \pm 1.28 \times 10^{15} cm^{-3}$ and the σ_{FCA} values from the reported literature. Most of the σ_{FCA} values reported in literature do not have uncertainties documented though the Δn_0 error will introduce one when computing α_{FCA}. To calculate α_{FCA} it is simply the product of these two values. To compare it to the work presented here, we use equations (4.9) or (4.6) with their

respective Δn_0 value at the wavelength reported in literature. Equations (4.9) and (4.6) will give us a range of α_{FCA} due to the uncertainties in the quantities measured. The table below summarizes this comparison.

Author	Wavelength (nm)	α_{FCA} (Literature) (cm^{-1})	α_{FCA} (This work) (cm^{-1})	Agree? (Y/N)
Svantesson et al. [32]	1064	0.085 ± 0.008	0.039 ± 0.016	N
Meitzer et al. [34]	1510	0.294 ± 0.027	0.095 ± 0.038	N
Boyd et al. [22]	1550	0.082 ± 0.010	0.101 ± 0.040	Y
Khabibrakhmanov et al. [20]	1550	0.084 ± 0.010	0.101 ± 0.040	Y
Gauster et al. [31]	2600	0.296 ± 0.026	0.368 ± 0.147	Y
Linnros et al. [33]	3390	0.435 ± 0.039	0.715 ± 0.286	Y

Table 3: A comparison between this work and literature for optical methods. Errors in literature values are computed only using the error in Δn_0. In the odd case where σ_{FCA} errors were reported such as in [22] and [20] they were considered.

Svantesson's predicted α_{FCA} value uses $\sigma_{FCA} = 4.9 \times 10^{-18}$ cm^2 at 1064 nm which appears to be an overestimation. When compared to the α_{FCA} value at 1064 nm for this work using equation (4.6) it is off by a factor of ~2. When compared to (4.9) it is off by a factor of ~3. At lower wavelengths, especially < 1100 nm the α_{FCA} seems to vary the most as shown in this work they are plagued with quite large uncertainties. Svantesson claims his value when scaled up to higher wavelengths agrees with Gauster's work at 2600 nm. We will see later Gauster's work agrees with this work in the long wavelength regime which potentially form an agreement among all previously mentioned values.

Meitzer's reports a value of $\sigma_{FCA} = 1.69 \times 10^{-17}$ cm^2 at 1510 nm and claims it agrees with Linnros and Gauster. However, I believe this does not make sense as Gauster reports a similar value of the $\sigma_{FCA} = 1.7 \times 10^{-17}$ cm^2 but at 2600 nm. If this was true, it would mean at the same Δn_0, the α_{FCA} value would be approximately the same at 1510 nm and 2600 nm as shown in Table 3, but this obviously cannot be true. Linnros reports a value of $\sigma_{FCA} = 2.5 \times 10^{-17}$ cm^2 at 3390 nm which is line

with Gauster. This work also agrees with Linnros's and Gauster's values within their uncertainties.

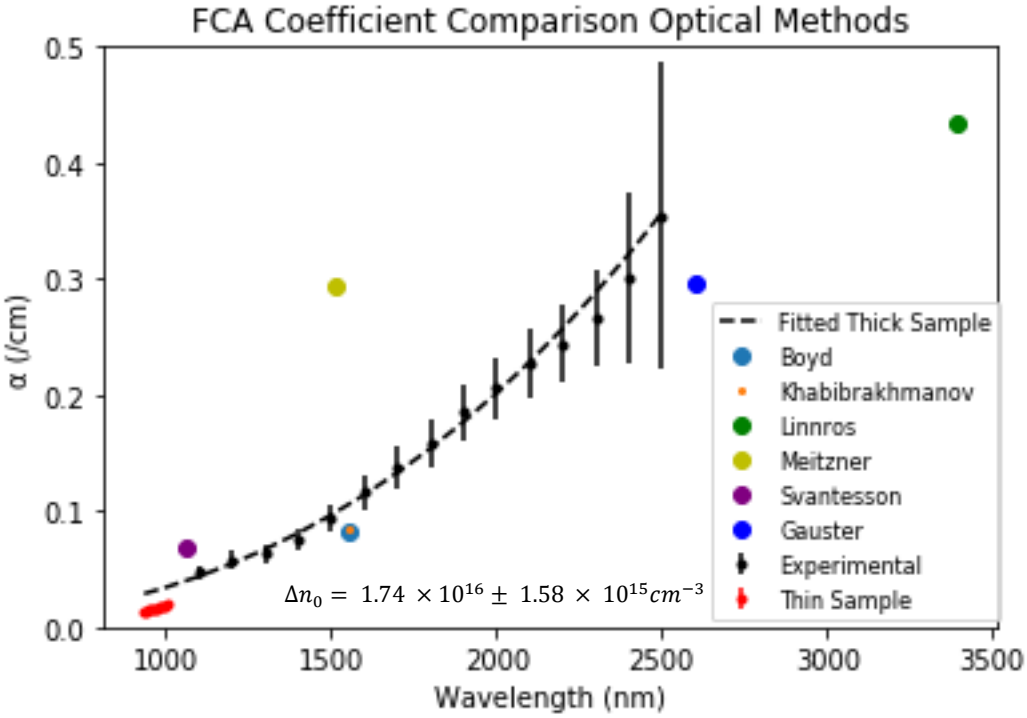

Figure 18: A comparison between this work and literature for the FCA Coefficient for optical methods.

Meitzner value as shown in Figure 14 is in too far of a disagreement with this work and other literature so it will be discarded for comparison's sake because of this large discrepancy. The values reported by Boyd and Khabibrakhmanov are very similar and agree with this work here as they should. The setup used in Khabibrakhmanov and this work was originally used by Boyd in his experiments. A few modifications have been implemented to better suit the experiment at hand but overall, the measurements and data collection process is the same.

We can now compare our results to the non-optical methods. In this case, the literature reported for non-optical methods provide parametrizations values for the generic fitting equation (3.3) presented in chapter 3 section 1.

$$\alpha_{FCA} = C_{FCA,n}\lambda^{\xi}\Delta n_0 \tag{3.3}$$

$$\alpha_{FCA,n} = C_{FCA,n}\lambda^{\delta} n \tag{4.10}$$

$$\alpha_{FCA,p} = C_{FCA,p}\lambda^{\varphi} p \tag{4.11}$$

Non-optical methods report separate equations $\alpha_{FCA,n}$ (4.10) and $\alpha_{FCA,p}$ (4.11) for n-type and p-type doping where the sum of them equals the true α_{FCA} (3.3) as shown in Drude theory. This accounts for the total number free carriers Δn_0 where n and p represent the excess concentrations for electrons and holes, respectively. The sum will be compared to equation (4.6) where we assumed excess electrons and holes are produced in a 1:1 ratio. The summed literature equations will be curve fit to equation (3.3) to extract new parameters (C_{FCA}, ξ) which can be compared to this work. The value of $\Delta n_0 = 1.74 \times 10^{16} \pm 1.58 \times 10^{15} cm^{-3}$ is used for the curve fits as the literature values are only reported in the wavelength range of 1000 nm to 2500 nm. A table of values (Table 4) and a plot (Figure 19) show the comparison among both methods.

Author	$C_{FCA}\Delta n_0$ (cm^{-3})	ξ	λ range (μm)	Δn_0 range (cm^{-3})
Rüdiger et al. [29]	6.00×10^8	2.49	1-2	~10^{17}-10^{20}
Drude [26] [27]	9.30×10^6	2.00	Any	Any
Green et al. [28]	3.57×10^9	2.66	<2.5	10^{18}
Xu et al. [30]	9.43×10^{10}	3	1-1.2	~10^{17}-10^{20}
Baker-Finch [5]	6.09×10^9	2.67	1-1.5	~10^{18}-5x10^{20}
This work	3.38×10^8	2.50 ± 0.06	1.1-2.5	~10^{16}

Table 4: A comparison between this work and literature for non-optical methods.

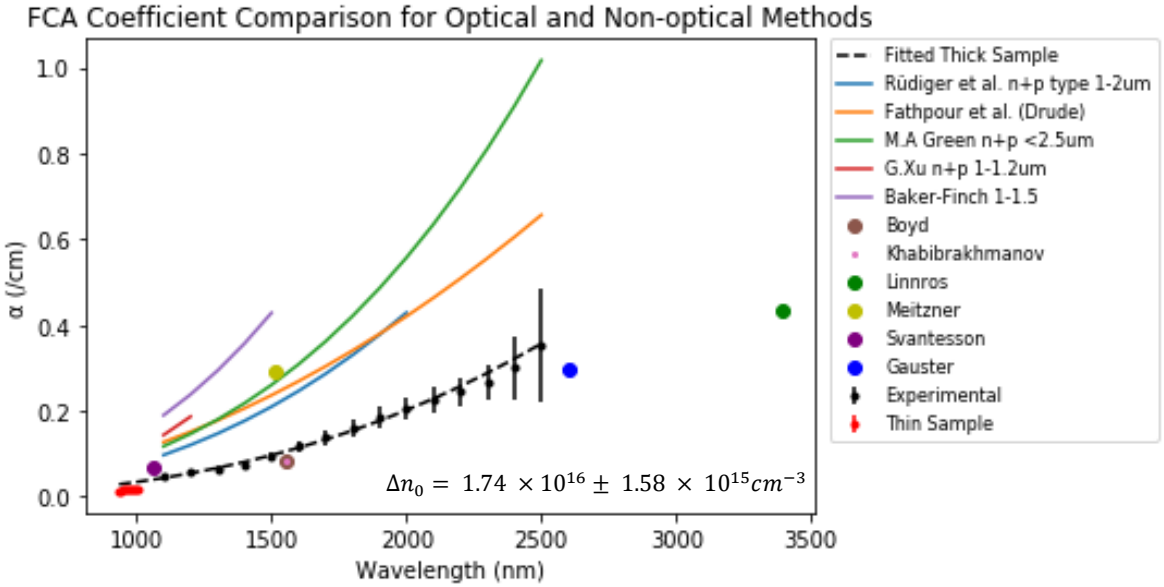

Figure 19: A comparison between this work and literature for the FCA Coefficient for optical and non-optical methods.

From Table 4 we can see the product of $C_{FCA}\Delta n_0$ is generally higher for the non-optical methods. We can visually see on Figure 19 that there is a clear 'separation' between the two methods. In non-optical methods, the fitting equations are parametrized on experimental data from samples with large Δn_0 values (10^{17}-10^{20} cm^{-3}). These equations are only valid within the range stated in Table 4, meaning using a Δn_0 outside the range such as ~10^{16} could have an invalid effect on the parametrization of C_{FCA}. Vice versa, if we assume a Δn_0 of ~10^{18} it would validate the non-optical parametrizations but could show inconsistency in this work as it has never been tested at such high Δn_0 values.

The value of ξ generally stays the same across both methods ranging from 2-3. This shows the curvature of each function behaves approximately the same. However, the Drude theory is an exception as it is a truly parabolic function. The Drude theory only considers scattering from acoustic phonons. It does not consider electron-hole scattering and scattering from impurities which seems to be the main reason for the discrepancies between the two methods.

Assuming that this work is valid at any arbitrary Δn_0 a 'separation' would always still be present between the two methods. A likely reason for this comes from the samples used and where the free carriers come from and how they are scattered. In this work, free carriers are optically injected using a pump beam in a 1:1 ratio whereas in non-optical methods carriers originate from dopants. For undoped or intrinsic doped samples, the process of light absorption by free carriers is governed through electron-hole scattering since a momentum-conserving scattering event is required for an intra-band transition. For doped samples, the dominant scattering mechanism is impurity scattering. Therefore, as Boyd points out the dominant scattering mechanism must influence the magnitude of the FCA cross-section in some way [6]. The scattering mechanisms that can be present are lattice, impurity and electron-hole scattering. Samples with diffused dopants undergo impurity scattering, the process of free carriers interacting with charge donor or acceptor atoms. In lightly doped samples where the free carriers are optically injected, the main scattering mechanism is electron-hole scattering in which free carriers interact with each other.

When a material is doped, an influx of free carriers and charge donor or acceptor atoms are present. As the number of free carriers increases, the probability for a scattering event will also increase. Therefore, the scattering time; the average time for a scattering event to occur, will decrease. A decrease in scattering time results in a decrease in carrier mobility which increases the FCA coefficient as per the Drude theory.

Klaassen reports that the cross-section due to impurity scattering is two times higher than electron-hole scattering for high carrier concentrations in silicon [35]. The model presented gives an analytical function for the carrier mobility as a function of donor, acceptor, electron, and hole concentrations and of the temperature. It considers contributions from lattice, donor, acceptor, and electron-hole scattering. By looking at the individual terms that describe the majority impurity scattering and electron-hole scattering we can see how they relate to each other. The model relies only on the carrier concentration and temperature as a variable and the rest is given by model parameters. In the model the electron and hole mobilities due to donor and accepter scattering, respectively, can be calculated. When determining the contributions from electron-hole scattering, a mobility ratio $F(P)$, can be computed which relates the mobilities from impurity scattering to the mobilities from carriers. $F(P)$ consists of many model parameters, including P which is a model parameter that depends on carrier concentration and temperature. The table below shows values that sweep through a carrier concentration range of 10^{16}-10^{20} cm^{-3} at a temperature of 300 K

Concentration (cm^{-3})	$\mu_{n,impurity}$ (cm^2/Vs)	$\mu_{p,impurity}$ (cm^2/Vs)	$F(P)_n$	$F(P)_p$	$\mu_{n,e-h}$ (cm^2/Vs)	$\mu_{p,e-h}$ (cm^2/Vs)
10^{16}	6942	4897	0.79	0.78	5484	3820
10^{17}	1493	976	0.88	0.82	1317	800
10^{18}	355	226	1.24	0.97	440	220
10^{19}	117	83	2.40	1.40	281	116
10^{20}	67	56	4.39	1.98	294	110

Table 5: A comparison between electron and hole mobilities from impurity scattering and carrier scattering at 300 K.

From Table 5, we can see that as the carrier concentration increases, the mobilities from impurity and electron-hole scattering decrease due to the decrease in scattering time as more scattering sites are present. At low concentrations (10^{16}-10^{18} cm^{-3}) the mobilities from impurity scattering are higher than the mobilities from electron-hole scattering. This isn't too relevant because there are no cases of low concentration of impurities reported. However, what is more relevant is at high concentrations (10^{18}-10^{20} cm^{-3}) where most non-optical methods are valid as shown in Table 4. At high concentrations, the mobilities from electron-hole scattering are higher compared to the mobilities from impurity scattering. We can use the Drude equation (3.1) from Chapter 3 to see the effect it has on the FCA coefficient.

For simplicity's sake we can assume $n = p$

$$\alpha_{FCA} = \frac{q^3\lambda^2}{4\pi^2\varepsilon_0 c^3 n}\left[\frac{n}{m_n^{*2}\mu_n} + \frac{p}{m_p^{*2}\mu_p}\right] \tag{3.1}$$

which turns the equation into:

$$\alpha_{FCA} = \frac{q^3\lambda^2}{4\pi^2\varepsilon_0 c^3 n} n\, M \tag{4.12}$$

where:

$$M = \frac{(m_n^{*2}\mu_n)(m_p^{*2}\mu_p)}{(m_n^{*2}\mu_n) + (m_p^{*2}\mu_p)} \tag{4.13}$$

In this case M represents the impact that the mobilities μ_n and μ_p have on α_{FCA}. This way we can apply the values from Table 5 to equation 4.13 to see how it effects α_{FCA}. This is summarized in the table below:

Concentration (cm^{-3})	$M_{impurity}$	M_{e-h}	$\frac{M_{impurity}}{M_{e-h}}$
10^{18}	1.99	1.98	1.00
10^{19}	5.51	3.68	1.50
10^{20}	8.40	3.84	2.19

Table 6: Comparison between the impact that the mobilities μ_n and μ_p have on α_{FCA} for impurity and electron-hole scattering at high concentrations

From Table 6, we can see that at a concentration of 10^{18} cm^{-3} the contributions on α_{FCA} from impurity and electron-hole scattering are almost equal however when you increase the concentration up to 10^{20} cm^{-3} impurity scattering is twice that of electron-hole scattering which can explain the discrepancies between optical and non-optical methods.

This makes sense because as the doping level increases, not only will there be more carriers to collide with and scatter, doping also introduces charge donor or acceptor atoms that can act as scattering sites. These additional sites are what makes the difference compared to electron-hole scattering. From this, we can conclude that non-optical methods would naturally produce higher α_{FCA} due to the additional scattering events induced by donor or acceptor atoms. Furthermore, donor or acceptor atoms are much much larger than carriers so you would expect the probability of a scattering event to increase in a given area simply because of how large atoms are compared to carriers. The scattering time would be shortened as a result, which would decrease the carrier mobility and increase the FCA coefficient.

5. Conclusion and Future Work

In this work, I have performed measurements in a completely optical approach to determine the FCA cross-section and the associated FCA coefficient over a range of wavelength that has yet to be explored in silicon. The effective lifetime of a sample is measured using MFCA pump-probe spectroscopy, where the pump and probe facilitate inter-band and intra-band absorption respectively. The probe can measure an induced FCA signal from a modulated pump beam which sweeps through a range of modulation frequencies to resemble a Lorentzian decay function from the probe's detector. The lifetime and AC probe signal amplitude can be extracted from a curve fit which are used as the primary experimental quantities when calculating the FCA cross-section and the associated FCA coefficient.

The wavelength range I achieved spans from 935 to 2500 nm. Single wavelength measurements using optical approaches have been reported in literature but never over a continuous range. Furthermore, no measurements below 1000 nm have been reported regardless of the method used until now. It has been found that there is a clear separation between the FCA cross-section and coefficient depending on how free carriers are injected into the conduction band.

For optical injection, carriers are introduced using a pump laser and are generated in a 1:1 ratio. For doped samples, carriers are injected using dopants which also introduces ionized impurities. The process of FCA requires a momentum conserving event to occur due to the parabolic nature of the conduction band. This event is in the form of scattering which can be electron-hole scattering for optical injection methods or impurity scattering for doped samples.

Optical injection results in a much higher degree of precision as stated by Boyd who performed similar experiments [6]. He states the signal is only sensitive to the periodic change in FCA population due to injection. This limits the measurement uncertainty down to just one quantity rather than the two quantities (the incident power, and the reflected/transmitted powers) for non-optical methods.

The FCA cross-section values reported in literature vary greatly and can be shown in Baker-Finch et al. summary report [5]. These values are also only reported in the higher wavelength and excess carrier concentration ranges. Baker-Finch claims there is a large experimental

uncertainty as the cross-section is a function of many parameters [5]. Another reason has to do with the dominant scattering mechanism. Klaassen reports that the cross sections for impurity scattering are two times higher than electron-hole scattering which tends to validate the results presented here [35].

Future work in this area of study would be to push the limits on the lower end of the wavelength range. Doing so would require thinner samples and an upgraded pump beam which could output more power. Thinner samples would require quinhydrone/methanol treatments to create a surface passivation effect that would increase lifetime and allow for measurements to be performed [38]. Lower wavelength ranges would correspond more to the primary operating wavelength ranges for solar cells. FCA acts as a loss mechanism, particularly in heavily doped devices operating in the infrared where FCA competes with traditional band to band transitions. This energy is wasted in the form of heat through thermalization in the upper energy levels of the conduction band. Understanding FCA at lower wavelengths could help improve the efficiency of solar cells.

6. References

[1] A. Blakers, "High Efficiency Silicon Solar Cells," *Energy Procedia,* vol. 33, pp. 1-10, 2013.

[2] F. Shimura, "Noncontact minority-carrier lifetime measurement at elevated temperatures for metal-doped Czochralski silicon crystals," *Journal of Applied Physics,* vol. 67, no. 11, pp. 7168-7171, 1990.

[3] V. Petrova-koch, High-Efficient Low-Cost Photovoltaics, Berlin: Springer Berlin Heidelberg, 2009.

[4] S. Rein, Lifetime Spectroscopy, Berlin: Springer Berlin Heidelberg, 2005.

[5] S. C. Baker-Finch, "Near-infrared free carrier absorption in heavily doped silicon," *Journal of Applied Physics,* vol. 116, no. 6, p. 063106, 2014.

[6] K. Boyd, "Free-Carrier Pump / Probe Spectroscopy," McMaster University, Hamilton, 2018.

[7] M. Kunst, "The study of charge carrier kinetics in semiconductors by microwave conductivity measurements," *Journal Of Applied Physics,* vol. 60, no. 10, p. 3358, 1986.

[8] J. S. Swirhun, "Contactless measurement of minority carrier lifetime in silicon ingots and bricks," *Prog. Photovoltaics Res. Appl,* vol. 19, no. 3, pp. 313-319, 2011.

[9] K. Sopian, "An overview of crystalline silicon solar cell technology: Past, present, and future,," p. 020004, 2017.

[10] L. Huldt, "Optical Method for Determining Carrier Lifetimes in Semiconductors," *Phys. Rev. Lett.,* vol. 2, no. 1, p. 3, 1959.

[11] N. G. Nilsson, "Determination of carrier lifetime, diffusion length, and surface recombination velocity in semiconductors from photo-excited infrared absorption," *Solid-State Electron,* vol. 7, no. 6, pp. 445-463, 1964.

[12] F. Sanii, "Contactless nondestructive measurement of bulk and surface recombination using frequency-modulated free carrier absorption," *Solid-State Electron,* vol. 35, no. 3, pp. 311-317, 1992.

[13] F. Sanii, "The Measurement of Bulk and Surface Recombination by Means of Modulated Free Carrier Absorption," *IEEE J. Photovolt,* p. 575.

[14] X. Zhang, "Carrier Diffusivity Measurement in Silicon Wafers Using Free Carrier Absorption," *Int. J. Thermophys,* vol. 34, no. 8-9, pp. 1721-1726, 2013.

[15] S. Ren, "Three-dimensional transient model for time-domain free-carrier absorption measurement of excess carriers in silicon wafers," *J. Appl. Phys,* vol. 114, no. 24, p. 243702, 2013.

[16] K. L. Luke, "Analysis of the interaction of a laser pulse with a silicon wafer: Determination of bulk lifetime and surface recombination velocity," *J. Appl. Phys,* vol. 61, no. 6, pp. 2282-2293, 1987.

[17] S. W. Glunz, "Injection-level-dependent recombination velocities at the Si-SiO 2 interface for various dopant concentrations," *J. Appl. Phys.,* vol. 75, no. 3, pp. 1611-1615, 1994.

[18] W. Seifert, "Influence of dislocation density on recombination at grain boundaries in multicrystalline silicon," *Semicond. Sci. Technol,* vol. 8, no. 9, p. 1687, 1993.

[19] S. Gao, Carrier Lifetime and Diffusion Measurement using Free-carrier Absorption Imaging, Hamilton: McMaster University, 2020.

[20] R. Khabibrakhmanov, Determination of Effective Lifetime and Light Trapping Enhancement in Silicon using Free Carrier Absorption, Hamilton: McMaster University, 2021.

[21] S. S. Suvanam, "4H-silicon carbide-dielectric interface recombination analysis using free carrier absorption,," *J. Appl. Phys,* vol. 117, no. 10, p. 105309, 2015.

[22] K. Boyd, "Quasi-Steady-State Free Carrier Absorption Measurements of Effective Carrier Lifetime in Silicon," *IEEE J. Photovoltaics,* vol. 9, no. 1, pp. 64-71, 2019.

[23] D. Schroder, "Free Carrier Absorption in Silicon," *IEEE JOURNAL OF SOLID-STATE CIRCUITS,* Vols. SC-13, no. 1, 1978.

[24] R. A. Smith, Semiconductors, New York : Cambridge, 1961.

[25] J. Isenberga, "Free carrier absorption in heavily doped silicon layers," *Applied Physics Letters,* vol. 84, no. 13, p. 2265, 2004.

[26] S. Fathpour, "Two-Photon Photovoltaic Effect in Silicon," *IEEE Journal of Quantum electronics,* vol. 43, no. 12, pp. 1211-1217, 2007.

[27] X. Sang, "Applications of two-photon absorption in silicon," *JOURNAL OF OPTOELECTRONICS AND ADVANCED MATERIALS,* vol. 11, no. 1, pp. 14-25, 2008.

[28] M. A. Green, Silicon Solar Cells: Advanced Principles and Practice, Sydney, Australia: University of New South Wales, 1995.

[29] M. Rüdiger, "Parameterization of Free Carrier Absorption in," *IEEE TRANSACTIONS ON ELECTRON DEVICES,* vol. 60, no. 7, pp. 2156-2163, 2013.

[30] G. Xu, "An improved optical simulation method for crystalline silicon solar cells," *Proceedings of the 39th IEEE Photovoltaic Specialists Conference,* pp. 2677-2680, 2013.

[31] W. B. Gauster, "Laser-Induced Infrared Absorption in Silicon," *Journal of Applied Physics,* vol. 41, no. 9, p. 3850, 1970.

[32] K. Svantesson, "Determination of the Absorption and the Free Carrier Distribution in Silicon at High Level Photogeneration at 1.06 μm and 294 K," *Physica Scripta,* vol. 18, pp. 405-409, 1978.

[33] J. Linnros, "Carrier lifetime measurements using free carrier absorption transients," *Journal of Applied Physics,* vol. 84, no. 1, 1998.

[34] J. Meitzner, "Time-resolved measurement of free carrier absorption, diffusivity,," *Applied Physics Letters,* no. 103, p. 092101, 2013.

[35] D. B. M. Klaassen, "A unified mobility model for device simulation—I. Model equations and concentration dependence," *Solid-State Electron,* vol. 35, no. 7, pp. 953-959, 1992.

[36] V. Grivickas, Carrier Lifetime: Free Carrier Absorption, Photoconductivity, and Photoluminescence, Hoboken, NJ, USA: John Wiley & Sons, 2012.

[37] Schinke, n, k 0.25-1.45 μm, 2015.

[38] H. T, "Quinhydrone/Methanol Treatment for the Measurement," *Japanese Journal of Applied,* vol. 41, pp. 870-872, 2002.

[39] O. Optronics, "NanaoScan Beam Profiler," https://www.ophiropt.com/laser--measurement/sites/default/files/NanoScan2s_2.pdf, 2021.

[40] F. Instruments, "MDPmap," https://www.freiberginstruments.com/upcdmdp/mdpmap.html.

[41] W. contributors, Second-harmonic generation, In Wikipedia, The Free Encyclopedia, 2021.

Appendix A: Error Propagation for α_{FCA}

The FCA Cross-section is given by:

$$\sigma_{\mathrm{FCA}} = \frac{s}{2\eta \mathrm{m} f_a P_{0,pu} \lambda_{pu} \tau} A_{pu} hc$$

The error in the cross-section is given by:

$$\delta\sigma_{\mathrm{FCA}} = \sigma_{\mathrm{FCA}} \sqrt{\left(\frac{\delta s}{s}\right)^2 + \left(\frac{\delta A_{pu}}{A_{pu}}\right)^2 + \left(\frac{\delta f_a}{f_a}\right)^2 + \left(\frac{\delta P_{0,pu}}{P_{0,pu}}\right)^2 + \left(\frac{\delta \lambda_{pu}}{\lambda_{pu}}\right)^2 + \left(\frac{\delta \tau}{\tau}\right)^2}$$

The mean excess carrier density is given by:

$$\Delta n_0 = \frac{2 f_a P_{0,pu} \lambda_{pu}}{W A_{pu} hc} \tau$$

The error in the mean excess carrier density is given by:

$$\delta\Delta n_0 = \Delta n_0 \sqrt{\left(\frac{\delta f_a}{f_a}\right)^2 + \left(\frac{\delta P_{0,pu}}{P_{0,pu}}\right)^2 + \left(\frac{\delta \lambda_{pu}}{\lambda_{pu}}\right)^2 + \left(\frac{\delta \tau}{\tau}\right)^2 + \left(\frac{\delta W}{W}\right)^2 + \left(\frac{\delta A_{pu}}{A_{pu}}\right)^2}$$

The FCA coefficient is given by:

$$\alpha_{FCA} = \sigma_{FCA} \Delta n_0$$

The error in the FCA coefficient is given by:

$$\delta\alpha_{FCA} = \alpha_{FCA} \sqrt{\left(\frac{\delta\sigma_{\mathrm{FCA}}}{\sigma_{\mathrm{FCA}}}\right)^2 + \left(\frac{\delta\Delta n_0}{\Delta n_0}\right)^2}$$

Appendix B: Sample Specifications

Wafer ID	Thickness (μm)	Resistivity (Ω cm)	Doping Density (cm^{-3})	Surface Coating	Surface Type	Growth Type
Thick	1470 ± 2	1-5	4.51×10^{14}	Native Oxide	Double-side polish	CZ
Thin	325 ± 2	1-10	3.2×10^{15}	Native Oxide	Double-side polished	FZ

Note: All the doped wafers are n-type phosphorus doped

Appendix C: NanoScan Beam Profiler

The NanoScan beam profiler from MKS Ophir Optronics was used to measure the beam profile and sizes. It uses a silicon detector, capable for wavelengths between 190-1100nm. It can measure with great accuracy between the ranges of 7µm to 2.3mm [39]. The area of the beams was calculated as eclipses.

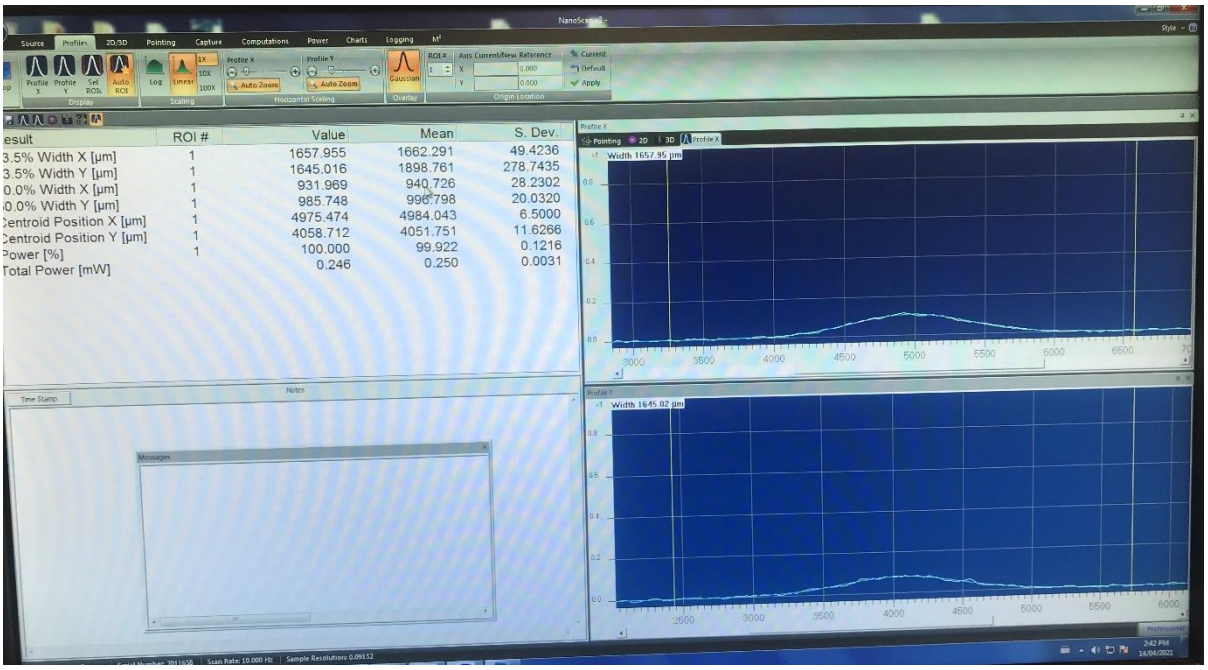

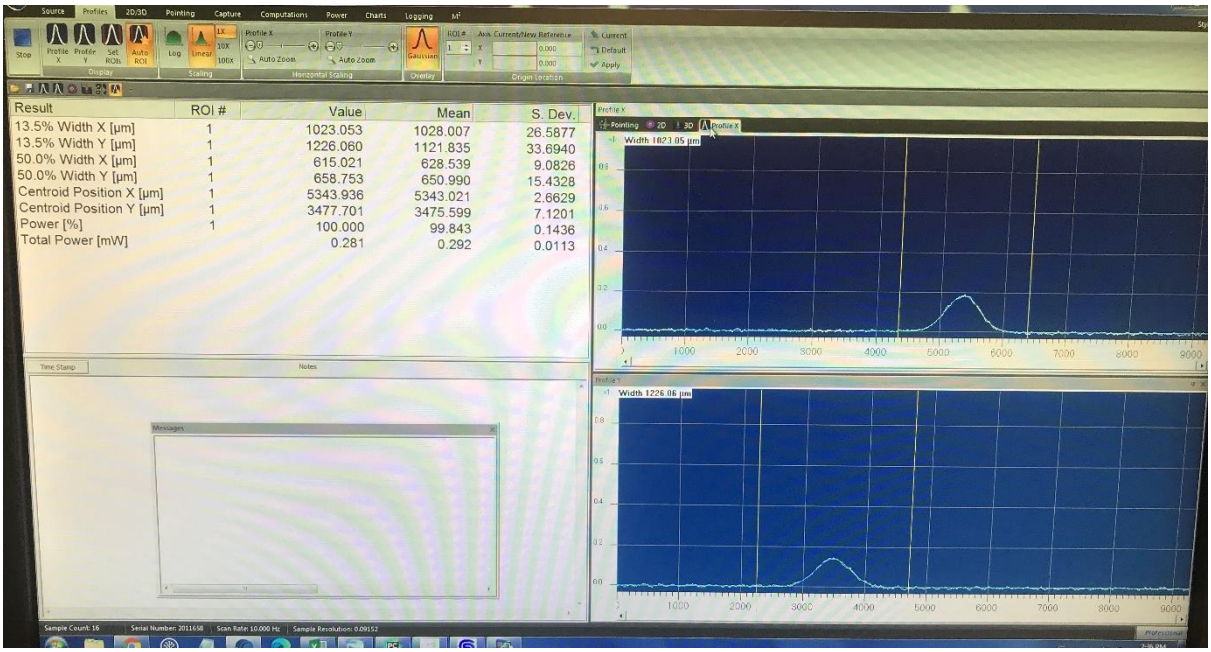

Appendix D: Lifetime Confirmation

The lifetime measurements were verified using the MDPmap from Freiberg Instruments [40]. This device measures lifetime from 20 ns – several ms for mono- and multi-crystalline wafers. It uses microwave photoconductance decay (μ-PCD) as described in Chapter 2. The thick and thin samples were measured to have lifetimes of approximately 100 μs and 30 μs respectively.

Appendix E: Decay Curves at all Wavelengths 935-2500 nm

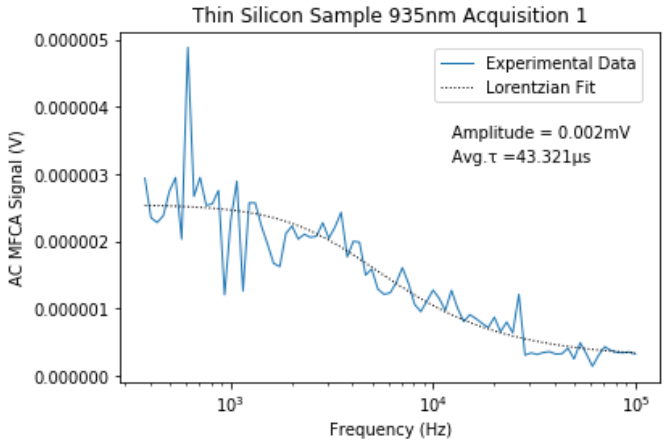

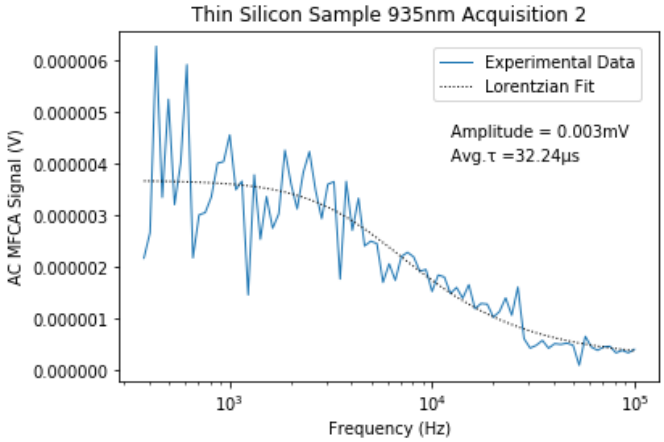

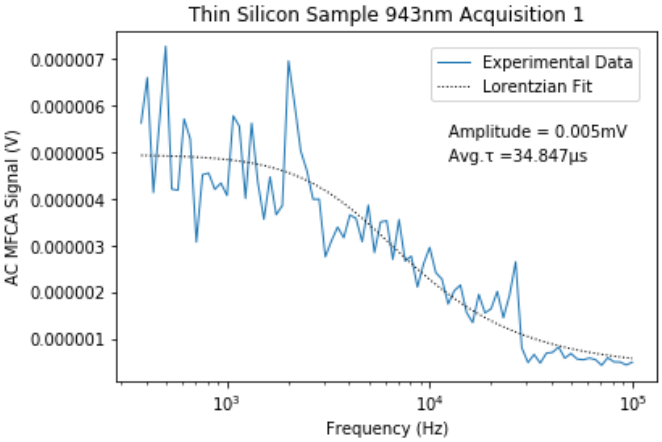

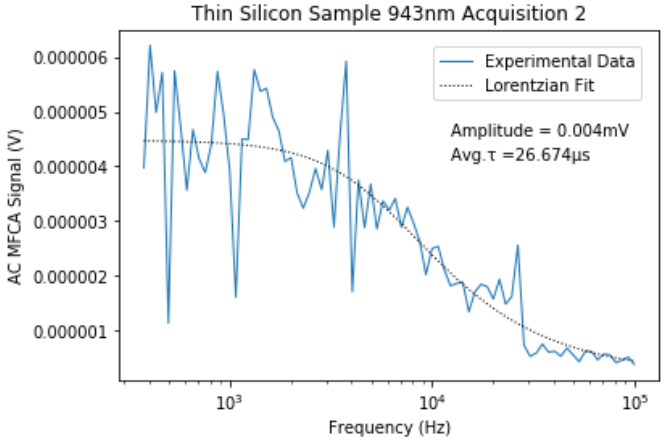

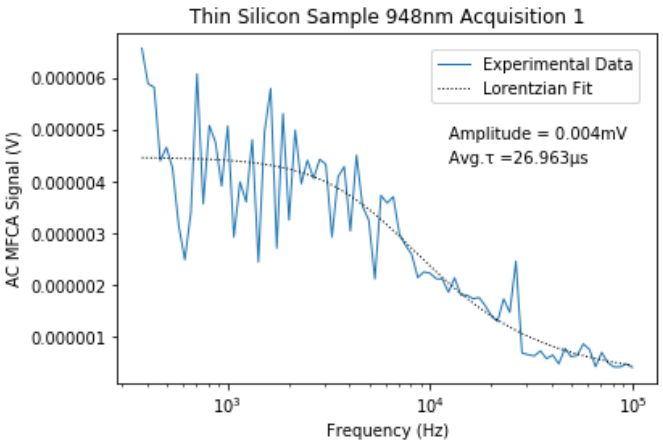

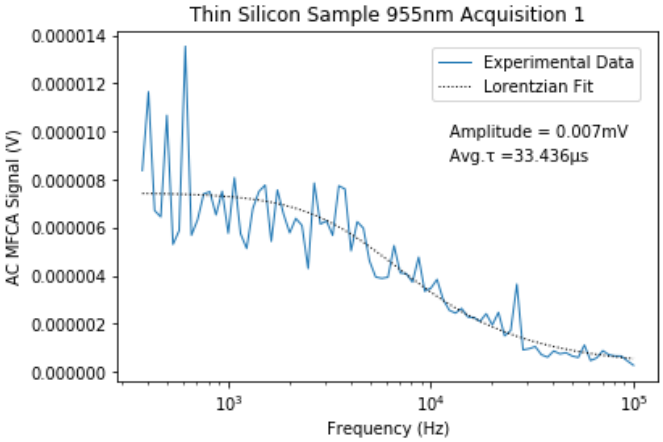

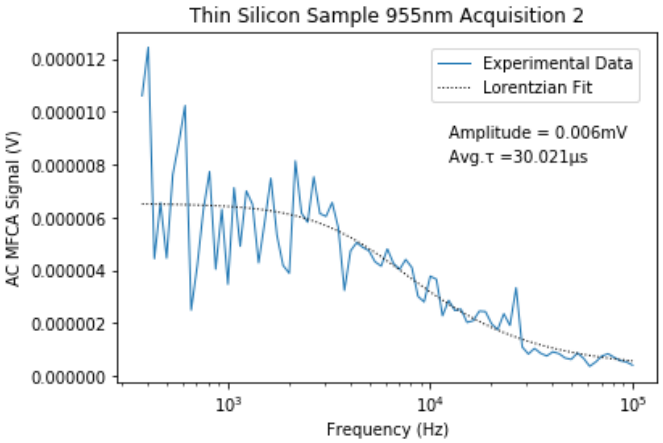
Thin Silicon Sample 955nm Acquisition 2
Experimental Data
Lorentzian Fit
Amplitude = 0.006mV
Avg.τ =30.021µs
AC MFCA Signal (V)
Frequency (Hz)

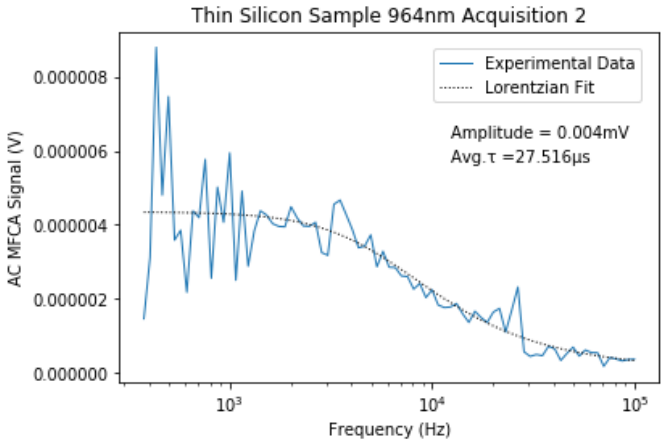
Thin Silicon Sample 964nm Acquisition 2
Experimental Data
Lorentzian Fit
Amplitude = 0.004mV
Avg.τ =27.516µs
AC MFCA Signal (V)
Frequency (Hz)

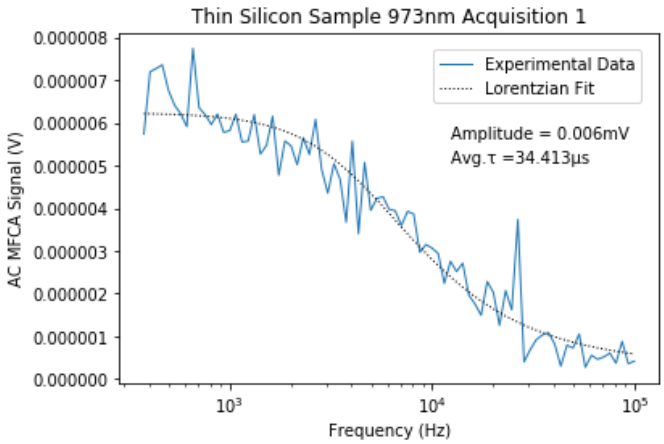
Thin Silicon Sample 973nm Acquisition 1
Experimental Data
Lorentzian Fit
Amplitude = 0.006mV
Avg.τ =34.413µs
AC MFCA Signal (V)
Frequency (Hz)

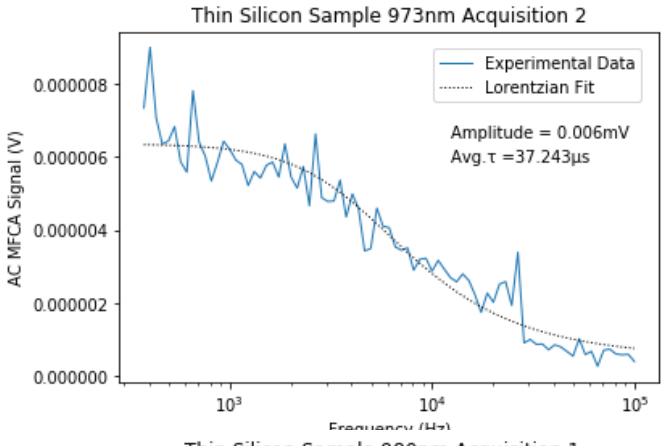
Thin Silicon Sample 973nm Acquisition 2
Experimental Data
Lorentzian Fit
Amplitude = 0.006mV
Avg.τ =37.243µs
AC MFCA Signal (V)

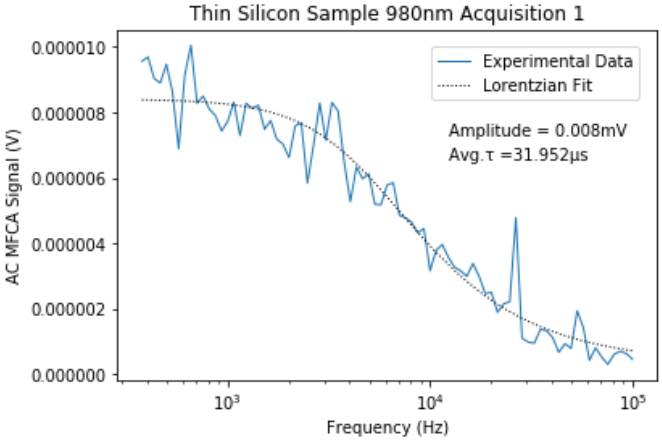
Thin Silicon Sample 980nm Acquisition 1
Experimental Data
Lorentzian Fit
Amplitude = 0.008mV
Avg.τ =31.952µs
AC MFCA Signal (V)
Frequency (Hz)

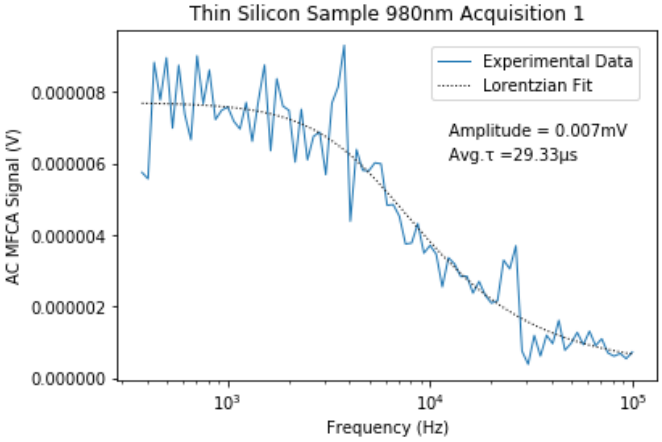
Thin Silicon Sample 980nm Acquisition 1
Experimental Data
Lorentzian Fit
Amplitude = 0.007mV
Avg.τ =29.33µs
AC MFCA Signal (V)
Frequency (Hz)

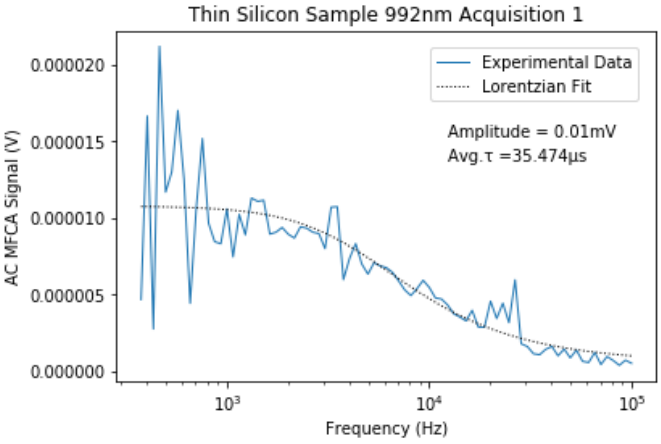
Thin Silicon Sample 992nm Acquisition 1
Experimental Data
Lorentzian Fit
Amplitude = 0.01mV
Avg.τ =35.474µs
AC MFCA Signal (V)
Frequency (Hz)

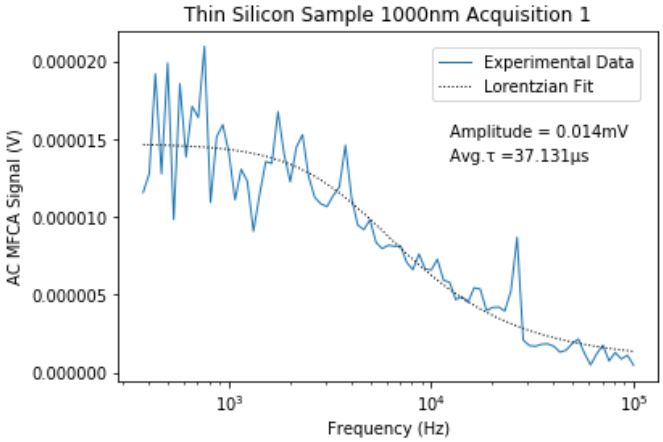
Thin Silicon Sample 1000nm Acquisition 1
Experimental Data
Lorentzian Fit
Amplitude = 0.014mV
Avg.τ =37.131µs
AC MFCA Signal (V)
Frequency (Hz)

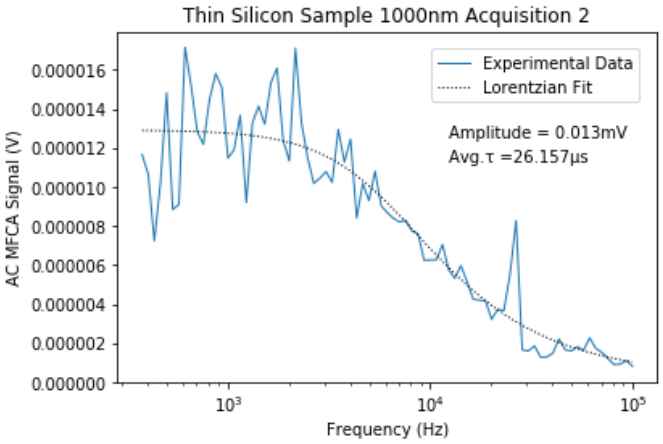
Thin Silicon Sample 1000nm Acquisition 2
Experimental Data
Lorentzian Fit
Amplitude = 0.013mV
Avg.τ =26.157μs
AC MFCA Signal (V)
Frequency (Hz)

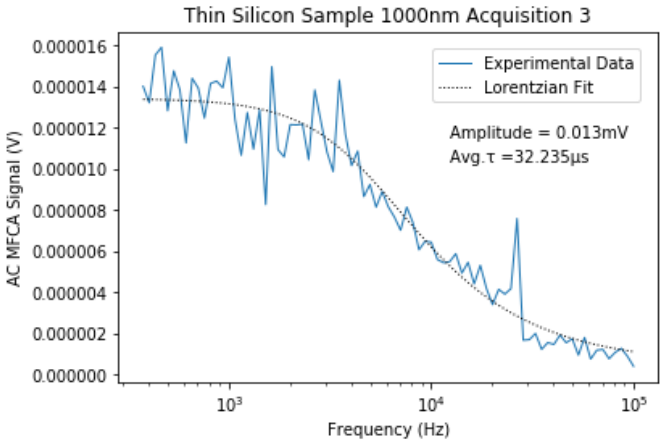
Thin Silicon Sample 1000nm Acquisition 3
Experimental Data
Lorentzian Fit
Amplitude = 0.013mV
Avg.τ =32.235μs
AC MFCA Signal (V)
Frequency (Hz)

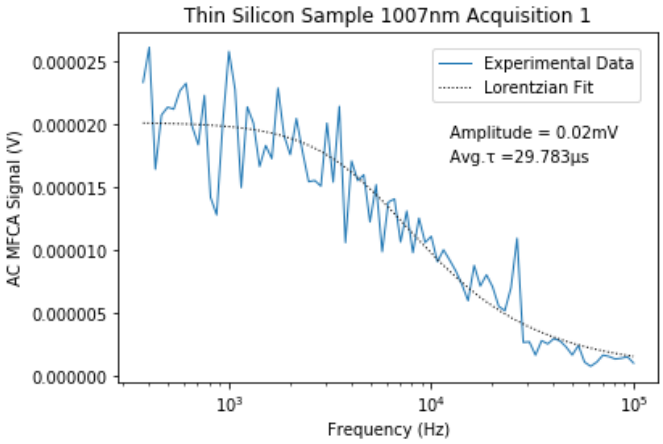
Thin Silicon Sample 1007nm Acquisition 1
Experimental Data
Lorentzian Fit
Amplitude = 0.02mV
Avg.τ =29.783μs
AC MFCA Signal (V)
Frequency (Hz)

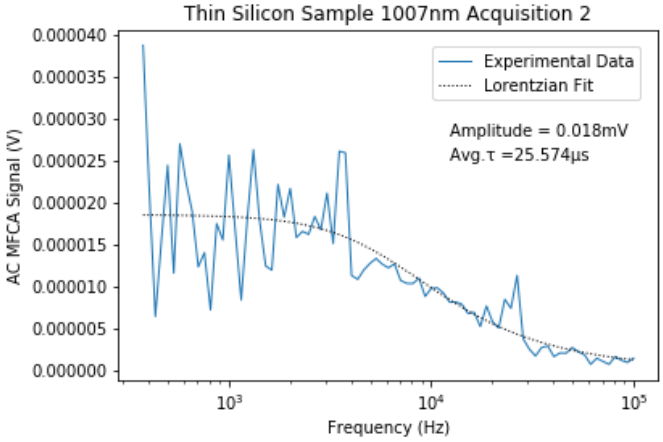
Thin Silicon Sample 1007nm Acquisition 2
Experimental Data
Lorentzian Fit
Amplitude = 0.018mV
Avg.τ =25.574μs
AC MFCA Signal (V)
Frequency (Hz)

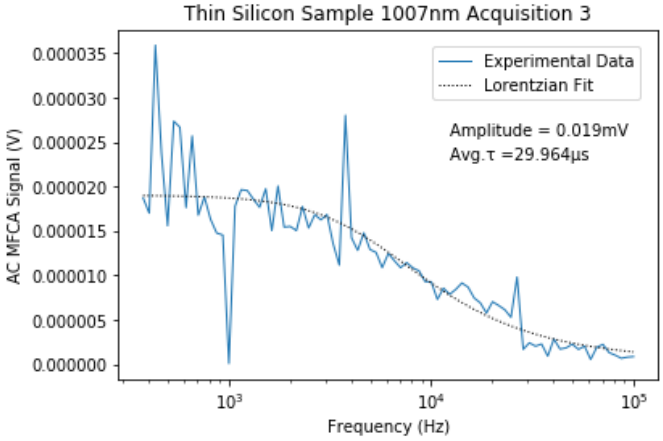
Thin Silicon Sample 1007nm Acquisition 3
Experimental Data
Lorentzian Fit
Amplitude = 0.019mV
Avg.τ =29.964μs
AC MFCA Signal (V)
Frequency (Hz)

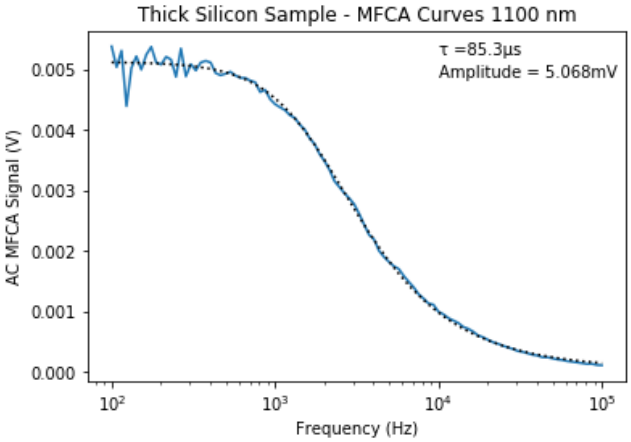
Thick Silicon Sample - MFCA Curves 1100 nm
τ =85.3µs
Amplitude = 5.068mV
AC MFCA Signal (V)
Frequency (Hz)

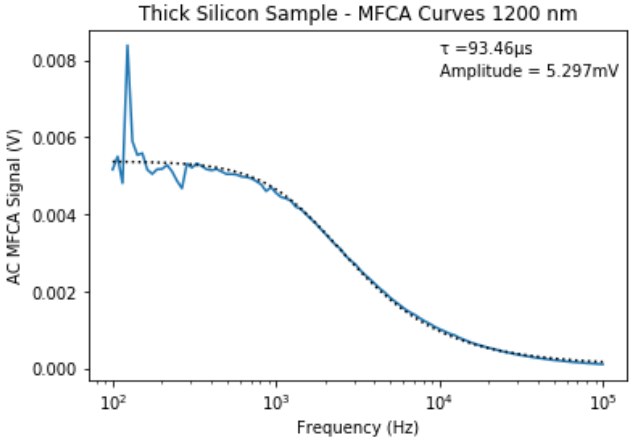
Thick Silicon Sample - MFCA Curves 1200 nm
τ =93.46µs
Amplitude = 5.297mV
AC MFCA Signal (V)
Frequency (Hz)

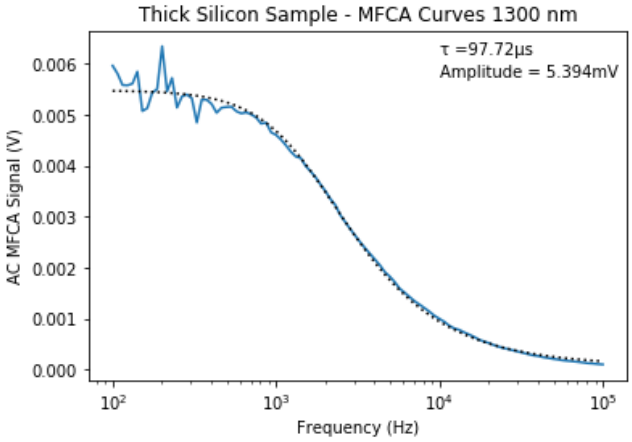
Thick Silicon Sample - MFCA Curves 1300 nm
τ =97.72µs
Amplitude = 5.394mV
AC MFCA Signal (V)
Frequency (Hz)

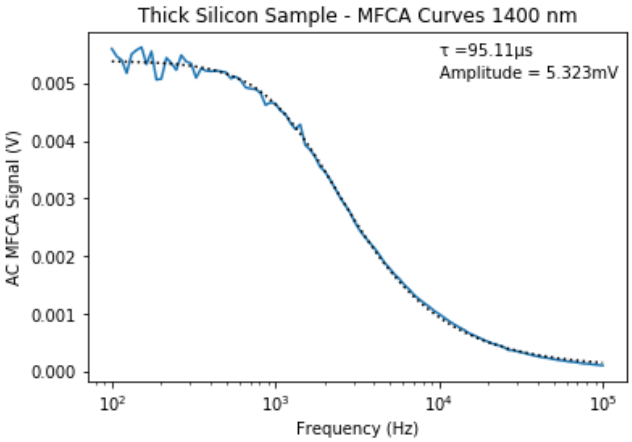
Thick Silicon Sample - MFCA Curves 1400 nm
τ =95.11µs
Amplitude = 5.323mV
AC MFCA Signal (V)
Frequency (Hz)

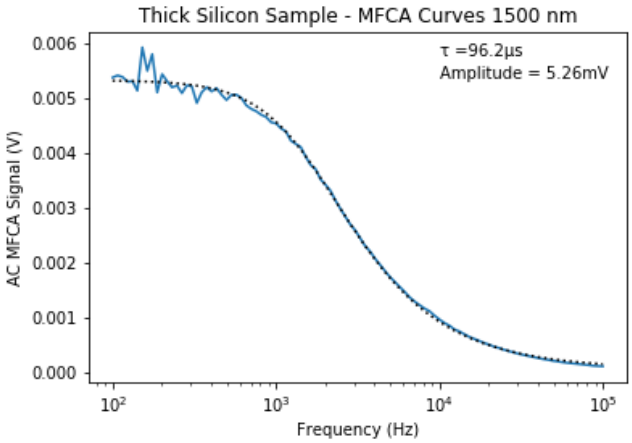
Thick Silicon Sample - MFCA Curves 1500 nm
τ =96.2µs
Amplitude = 5.26mV
AC MFCA Signal (V)
Frequency (Hz)

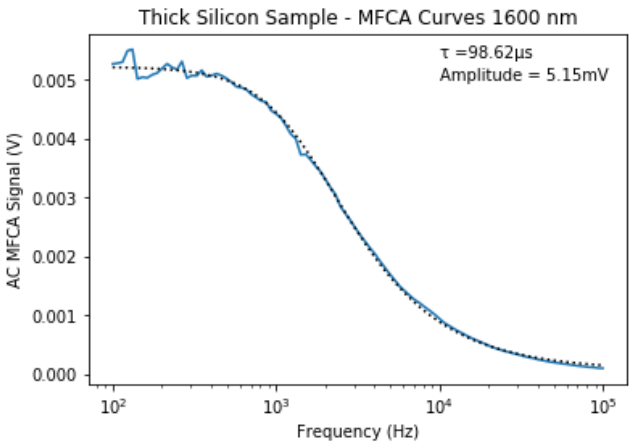
Thick Silicon Sample - MFCA Curves 1600 nm
τ =98.62µs
Amplitude = 5.15mV
AC MFCA Signal (V)
Frequency (Hz)

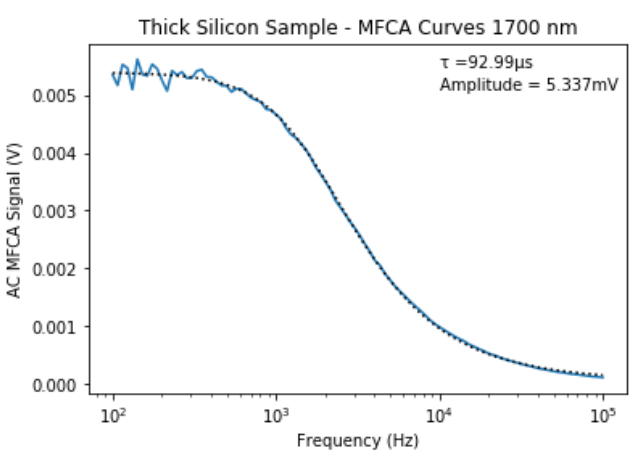
Thick Silicon Sample - MFCA Curves 1700 nm
τ =92.99µs
Amplitude = 5.337mV
AC MFCA Signal (V)
Frequency (Hz)

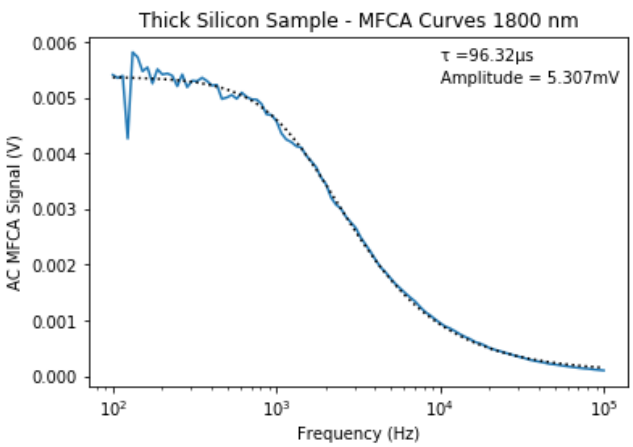
Thick Silicon Sample - MFCA Curves 1800 nm
τ =96.32µs
Amplitude = 5.307mV
AC MFCA Signal (V)
Frequency (Hz)

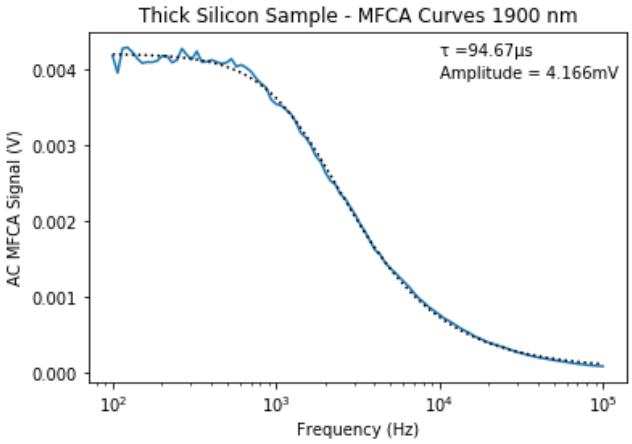
Thick Silicon Sample - MFCA Curves 1900 nm
τ =94.67µs
Amplitude = 4.166mV
AC MFCA Signal (V)
Frequency (Hz)

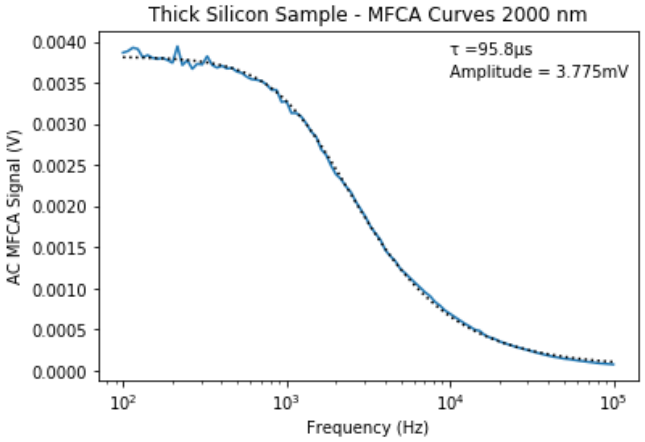
Thick Silicon Sample - MFCA Curves 2000 nm
τ =95.8µs
Amplitude = 3.775mV
AC MFCA Signal (V)
Frequency (Hz)

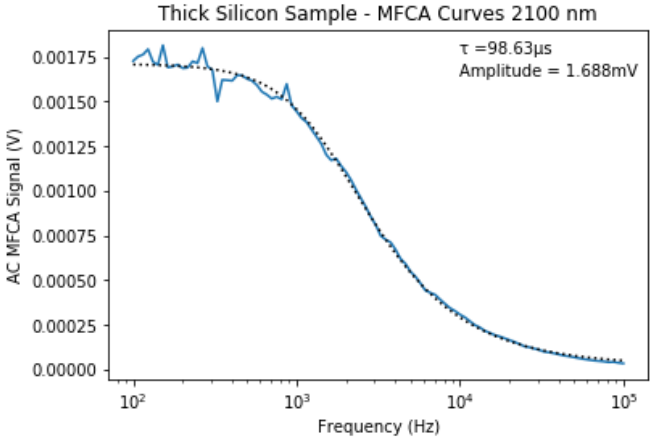
Thick Silicon Sample - MFCA Curves 2100 nm
τ =98.63µs
Amplitude = 1.688mV
AC MFCA Signal (V)
Frequency (Hz)

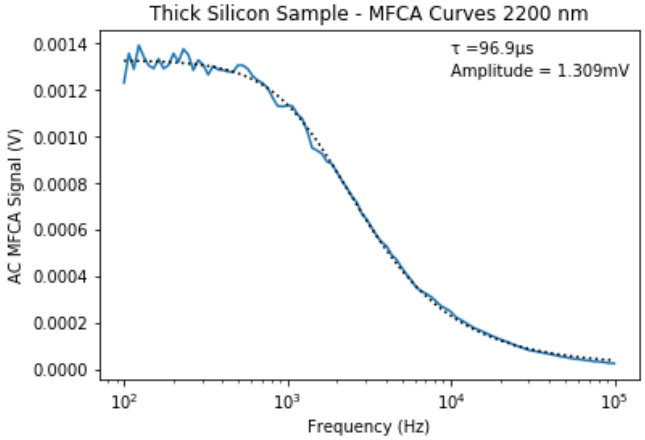
Thick Silicon Sample - MFCA Curves 2200 nm
τ =96.9µs
Amplitude = 1.309mV
AC MFCA Signal (V)
Frequency (Hz)

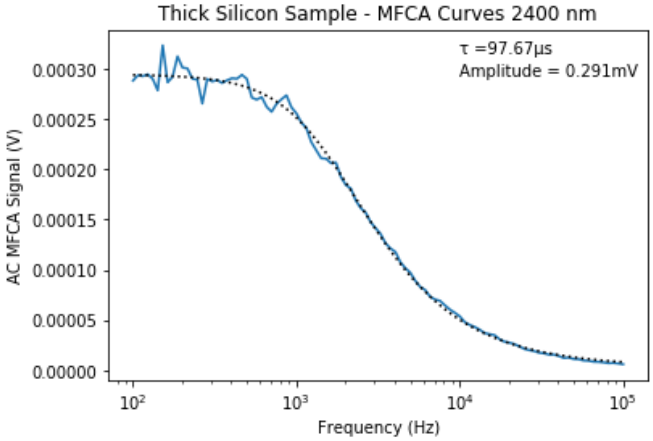
Thick Silicon Sample - MFCA Curves 2400 nm
τ =97.67µs
Amplitude = 0.291mV
AC MFCA Signal (V)
Frequency (Hz)

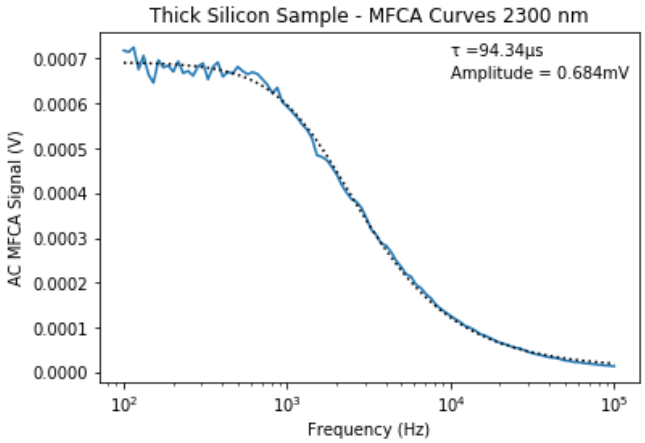
Thick Silicon Sample - MFCA Curves 2300 nm
τ =94.34µs
Amplitude = 0.684mV
AC MFCA Signal (V)
Frequency (Hz)

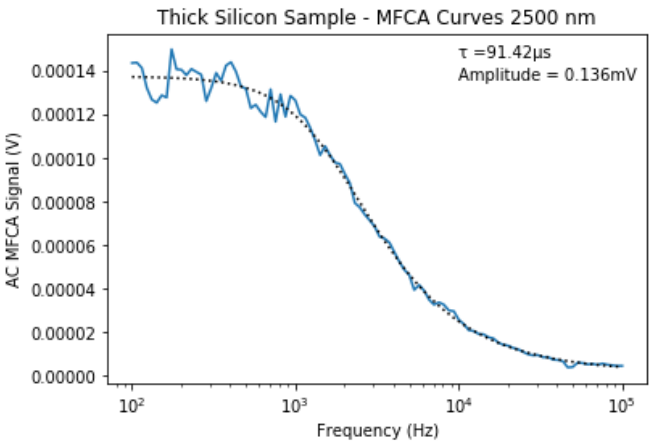
Thick Silicon Sample - MFCA Curves 2500 nm
τ =91.42µs
Amplitude = 0.136mV
AC MFCA Signal (V)
Frequency (Hz)